

Treatment and Resource Recovery

Tuning of Persulfate Activation from Free Radical to Non-Radical Pathway through the Incorporation of Non-Redox Magnesium Oxide

Ali Jawad, Kun Zhan, Haibin Wang, Ajmal Shahzad, Zehua Zeng,
Jia Wang, Xinquan Zhou, Habib Ullah, Zhulei Chen, and Zhuqi Chen

Environ. Sci. Technol., **Just Accepted Manuscript** • DOI: 10.1021/acs.est.9b04696 • Publication Date (Web): 23 Jan 2020

Downloaded from pubs.acs.org on January 24, 2020

Just Accepted

“Just Accepted” manuscripts have been peer-reviewed and accepted for publication. They are posted online prior to technical editing, formatting for publication and author proofing. The American Chemical Society provides “Just Accepted” as a service to the research community to expedite the dissemination of scientific material as soon as possible after acceptance. “Just Accepted” manuscripts appear in full in PDF format accompanied by an HTML abstract. “Just Accepted” manuscripts have been fully peer reviewed, but should not be considered the official version of record. They are citable by the Digital Object Identifier (DOI®). “Just Accepted” is an optional service offered to authors. Therefore, the “Just Accepted” Web site may not include all articles that will be published in the journal. After a manuscript is technically edited and formatted, it will be removed from the “Just Accepted” Web site and published as an ASAP article. Note that technical editing may introduce minor changes to the manuscript text and/or graphics which could affect content, and all legal disclaimers and ethical guidelines that apply to the journal pertain. ACS cannot be held responsible for errors or consequences arising from the use of information contained in these “Just Accepted” manuscripts.

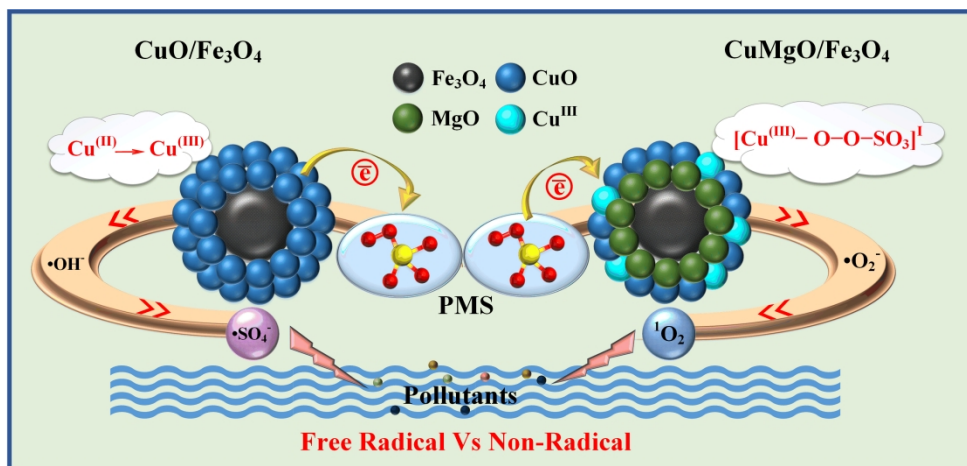


Table of content: The incorporation of MgO tunes the persulfate based oxidation from a classic radical process to a non-radical process

313x145mm (300 x 300 DPI)

1 Tuning of Persulfate Activation from Free Radical
2 to Non-Radical Pathway through the Incorporation
3 of Non-Redox Magnesium Oxide

4 Ali Jawad,^{1,2} Kun Zhan,¹ Haibin Wang,² Ajmal Shahzad,¹ Zehua Zeng,² Jia Wang,¹ Xinquan
5 Zhou,¹ Habib Ullah,³ Zhulei Chen,¹ and Zhuqi Chen,^{*2}

6

7 ¹ Hubei Provincial Engineering Laboratory of Solid Waste Treatment, Disposal and Recycling,
8 School of Environmental Science and Engineering, Huazhong University of Science and
9 Technology, Wuhan 430074, P. R. China

10 ² Key Laboratory of Material Chemistry for Energy Conversion and Storage, Ministry of
11 Education; Hubei Key Laboratory of Material Chemistry and Service Failure, School of
12 Chemistry and Chemical Engineering, Huazhong University of Science and Technology,
13 Wuhan 430074, PR China.

14 ³ Environment and Sustainability Institute (ESI), University of Exeter, Penryn Campus, Penryn,
15 Cornwall TR109FE, United Kingdom.

16 * Corresponding author

17 E-mail address: zqchen@hust.edu.cn.

18

19 **ABSTRACT:** Nonradical-based advanced oxidation processes for pollutants removal have
20 attracted much attention due to their inherent advantages. Herein we report that magnesium
21 oxides (MgO) in CuOMgO/Fe₃O₄ not only enhanced the catalytic properties but also switched
22 the free radical peroxymonosulfate-activated process into the ¹O₂ based nonradical process.
23 CuOMgO/Fe₃O₄ catalyst exhibited consistent performance in a wide pH range from 5.0 to 10.0,
24 and the degradation kinetics were not inhibited by the common free radical scavengers, anions
25 or natural organic matter. Quantitative structure activity relationships (QSARs) revealed the
26 relationship between the degradation rate constant of 14 substituted phenols and their
27 conventional descriptor variables (i.e. Hammett constants σ , σ^- , σ^+), half-wave oxidation
28 potential ($E_{1/2}$) and pK_a values. QSARs together with kinetic isotopic effect (KIE) recognized
29 the electron transfer as the dominant oxidation process. Characterizations and DFT calculation
30 indicated that the incorporated MgO alters the copper sites to highly oxidized metals centers,
31 offering a more suitable platform for PMS to generate metastable copper intermediates. This
32 highly oxidized metals centers of copper played the key role in producing O₂^{•-} after accepting
33 electron from another PMS molecule, and finally ¹O₂ as sole reactive species was generated
34 from the direct oxidation of O₂^{•-} through thermodynamically feasible reactions.

35 **KEYWORDS:** PMS, nonredox metals, singlet oxygen, nonradical, organic contaminants

36

37 Introduction

38 The worldwide water and soil pollution demanded strongly to develop an effective
39 remediation technology. Recently, chemical oxidation based on peroxymonosulfate (PMS) or
40 peroxydisulfate (PDS) activation has attracted many research groups owing to the generation
41 of powerful hydroxyl ($\bullet\text{OH}$), sulfate ($\text{SO}_4^{\bullet-}$) or both radicals.¹⁻⁵ Various strategies such as
42 light, heat, ultrasound, electricity and transition metals can be adopted to generate these radicals
43 during the activation of persulfate.¹⁻¹⁰ Among various strategies, transition metals (Co^{2+} , Fe^{2+} ,
44 Cu^{2+} , Mn^{2+}), their oxides (Co_3O_4 , Fe_3O_4 , CuO , MnO_2) and bimetallic composites (CuFe_2O_4 ,
45 $\text{CuO-Fe}_3\text{O}_4$, $\text{Mn}_{1.8}\text{Fe}_{1.2}\text{O}_4$ etc.) were recognized as the most efficient approaches.⁴⁻¹¹ In addition,
46 the persulfate activation through a similar pathway can also be achieved using biochar, reduced
47 graphene oxides, carbon nanotubes and N-doped graphene.¹²⁻¹⁵

48 The effectiveness of advance oxidation systems ($\text{H}_2\text{O}_2/\text{PMS}/\text{PS}$) relies on the strong oxidizing
49 power of free radicals (hydroxyl $\bullet\text{OH}$ E^0 1.9–2.7 V and sulfate $\text{SO}_4^{\bullet-}$ E^0 2.5–3.1 V) towards a
50 broad spectrum of recalcitrant pollutants.¹²⁻¹⁷ However, it can cause undesirable catalytic
51 durability due to its high reactivity for both the target compounds and competing
52 organic/inorganic constituents of water.¹⁸⁻²⁰ Meanwhile, the difficulty in the regeneration of
53 active sites due to the energetically unfavorable redox cycles is also considered one of the
54 major drawback in their practical application.

55 Alternately, the recently discovered non-radical oxidative pathway is highly selective for
56 electron rich organic pollutants, which can reduce the amount of side products.²¹⁻²³ The non-
57 radical process requires small amount of oxidants, and the degradation kinetics were less
58 influenced by the competing organic/inorganic constituents or radical scavengers.²² Non-
59 radical oxidative pathway can be broadly categorized into surface activated complex, electron
60 transfer mediation and singlet oxygen. The surface activated complex is resulted from the

61 activation of persulfates at the surface of catalysts and is considered completely different from
62 the free radical oxidation. For example, copper oxides were reported to generate surface
63 metastable complex during the activation of PDS,²¹ where the degradation kinetic of 2,4-
64 dichlorophenol was unaffected by excess amounts of Cl⁻ ions or radical scavengers. Similarly,
65 Pd-Al₂O₃ catalyst mediated electron transfer from organics to PMS, and such persulfate driven
66 activation exhibited a substrate selectivity which was similar to the carbon nano-tube/PMS
67 system.²²⁻²³ In contrast, a substrate selective surface-bound SO₄^{•-} radical mechanism was
68 proposed for Pd-Al₂O₃/PMS system, where the degradation kinetic of 1,4-dioxane was strongly
69 scavenged by radicals scavengers.²⁴ Contradicting to these reports, certain recent studies have
70 reported the presence of singlet oxygen (¹O₂) as another type of nonradical process.²⁵⁻³² The
71 ¹O₂-based pathway is also popular for their resistance to popular scavengers and background
72 substances in water matrix.

73 Using metal oxides, we recognized that there is a great deal of uncertainty regarding the
74 identification of reactive species. For example, CuO alone or its composite with the oxides of
75 other metals is reported to produce •SO₄⁻, •OH, surface bound complex or singlet oxygen
76 during persulfate activation.^{8,21,29,33} Similar kind of uncertainty also exist for the oxides of other
77 metals,^{22,23,26,31-32,34} reflecting that the mechanism behind the identification of reactive species
78 is ambiguous which needs further explorations. Most importantly, it is unclear that how the
79 reaction pathway changes, how non-radical ¹O₂-PMS activation dominate and how it
80 contributes in the degradation process yet to be answered.

81 In this work, we surprisingly found that the incorporation of magnesium oxides (MgO) onto
82 typical CuO/Fe₃O₄ catalyst not only enhanced the catalytic properties, but also switched the
83 free radical peroxymonosulfate-activated process into the ¹O₂ based nonradical process. There
84 is an urgent need to explain not only the positive aspects of MgO in catalysis but also disclose
85 the deeper insight behind the ¹O₂-based nonradical activation of PMS. Based on various

86 spectroscopic evidences and DFT calculations, the switching of reaction mechanism was
87 related to the transfer of Cu ions into highly electron deficient state and presence of extensive
88 surface OH groups after the incorporation of MgO. Furthermore, chemical scavenger tests,
89 EPR observation, the solvent dependency, FFA degradation as $^1\text{O}_2$ -indicator, pH studies,
90 complexation behaviors and the comparison with Rose Bengal (RB), a well-known $^1\text{O}_2$ -photo
91 sensitize system,³⁵ were conducted to address the knowledge gap in the identification and
92 generation mechanism of $^1\text{O}_2$ in CuOMgO/Fe₃O₄+PMS system. The linear free energy
93 relationships (LFERs) between the degradation rate constants of 14 substituted phenols and
94 conventional descriptor variables (i.e. Hammett constant σ , σ^- , σ^+), quantitative structure
95 activity relationship (QSARs) and kinetic isotopic effect (KIE) revealed the electron transfer
96 between the organic substrate in singlet oxygen dominated process.

97 **Materials and Methods**

98 **Materials Preparation**

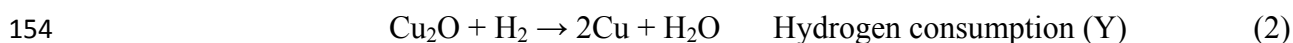
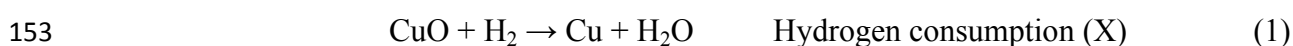
99 Copper and magnesium oxides were deposited on the surface of Fe₃O₄ by a simple
100 coprecipitation method. First, 100 mL Mg(NO₃)₂·6H₂O and Cu(NO₃)₂·6H₂O mixed solution in
101 different compositions (Table S1) were drop wisely added to 0.4 M (100 mL) Na₂CO₃ aqueous
102 solution containing 0.5 g of Fe₃O₄ (fixed amount), maintained at 60 °C over a time of 3 hours
103 (h). The prepared catalysts were dried at 80 °C, calcined at 500 °C for 5 h and named as shown
104 in Table S1. For the purpose of comparison, other catalysts CuO, Fe₃O₄, Co₃O₄, MnO₂, their
105 composite with Fe₃O₄ (i.e. CuO/Fe₃O₄, Co₃O₄/Fe₃O₄, MnO₂/Fe₃O₄), MgO incorporated
106 catalysts (i.e. Co₃O₄MgO/Fe₃O₄, MnO₂MgO/Fe₃O₄) or replacing MgO with the oxides of other
107 divalent metals (i.e. CuOCaO/Fe₃O₄, CuOBaO/Fe₃O₄, CuOZnO/Fe₃O₄) or transition metal
108 (CuOC₃O₄/Fe₃O₄) and replacing Fe₃O₄ with other support (i.e. CuOMgO/Al₂O₃ and
109 CuOMgO/SiO₂) were also prepared using the method mentioned earlier.

110 **Procedure for Pollutant Degradation**

111 The degradation of various organic compounds (O.Cs) was conducted in 30 mL glass bottles
112 under magnetic stirring. Different parameters such as the initial reaction pH, typical
113 background water constituents i.e. Cl^- , NO_3^- , SO_4^{2-} , CO_3^{2-} , HCO_3^- , HPO_4^- , humic acid (HA),
114 kinetics of OCs degradation, decomposition of PMS, oxidation products, recyclability,
115 leaching of active sites, toxicity based on the generation of BrO_3^- , structure activity relationship
116 by considering the degradation of 14 substituted phenolic compounds and kinetic isotopic
117 effect (KIE) were evaluated. Reactions were initiated at uncontrolled initial pH after adding
118 PMS, catalyst and 4-chlorophenol (4-CP) or other substituted OCs in desired concentration
119 with or without a constituent of interest (Cl^- , NO_3^- , SO_4^{2-} , CO_3^{2-} , HCO_3^- , HPO_4^- and HA).
120 Periodically, 1 mL sample was withdrawn, filtered with a 0.2 μM filter (polytetrafluoroethylene
121 syringe filters) and quenched immediately with excess ethanol before analyzing on HPLC. To
122 evaluate the consistent performance at wide effective pH, Rose Bengal (RB) as typical $^1\text{O}_2$ -
123 generator was also applied for the degradation of 4-CP.³⁵ The photosensitized process was
124 conducted in 100 mL quartz reactor at different initial pH, using 0.2 mM of RB and light
125 intensity of 280 mW/cm^2 . The generation of toxic BrO_3^- as byproduct in brominated medium
126 was analyzed by an ion chromatographic method as reported previously.³⁶ The zero point
127 charge of catalysts were determined by zeta potential method. To analyse the degradation
128 products of 4-CP on GC-MS, the reaction solution was dried first in freeze drier. The resulted
129 residue was transferred into 10 mL ethyl acetate and then passed through a sodium sulfate
130 packed column to remove the traces of water. The eluent was then concentrated under Ar
131 stream. To derivatized the degradation product, 0.1 mL MSTFA (a derivatizing agent) was
132 added and then followed by heating at 80 °C for 30 min. Similarly, the PMS concentration after
133 reaction was determined by UV-visible spectrometer as reported previously.³⁷ In general
134 procedure, 100 μL from sample or standard solutions were added into 10 mL mixed solution of

135 KHCO_3 and KI (1.25 g KHCO_3 + 10 g KI dissolved in 250 mL deionized water). The
 136 subsequent solution were initially hand shake and then analysed on UV-visible spectrometer at
 137 352 nm after reacting for 15 min.

138 To detect the reactive oxygen species (ROS), chemical scavengers like ethanol, tertiary butyl
 139 alcohol (TBA), benzoquinone (BQ), sodium azide (NaN_3) and furfural alcohol (FFA) were
 140 applied. To confirm the findings of chemical scavengers, electron paramagnetic resonance
 141 (EPR) spectroscopy with spin trapping reagents such as 2,2,6,6-tetramethyl-4-piperidone
 142 (TEMP) and 5,5-dimethyl-pyrroline-oxide (DMPO) were applied both in water and ethanol.
 143 Additionally, singlet oxygen as sole reactive species was further confirmed after considering
 144 FFA degradation, exchanging H_2O with D_2O and detection of H_2O_2 . The redox properties of
 145 the $\text{CuOMgO/Fe}_3\text{O}_4$ and $\text{CuO/Fe}_3\text{O}_4$ catalysts were determined by the hydrogen temperature
 146 programmed reduction method (H_2 -TPR).³⁸⁻³⁹ Initially, the solid $\text{CuOMgO/Fe}_3\text{O}_4$ and
 147 $\text{CuO/Fe}_3\text{O}_4$ catalysts were heated to 350 °C in a quartz reactor under an N_2 flow for 1 h. After
 148 cooling the samples to room temperature, the catalysts were reheated to 350 °C (10°/min) in
 149 the presence of a reducing agent (10% N_2/H_2 mixture), and the H_2 consumption was calculated
 150 (denoted X in Eq. 1). After cooling the catalyst to 50 °C, the surface copper was reoxidized for
 151 0.5 h in the presence of 20% $\text{N}_2\text{O}/\text{N}_2$. Finally, the second H_2 consumption was determined as
 152 described in the same way as the first H_2 -TPR (denoted Y in Eq. 2).



155 The exposed CuO_x surface area (S) and density of surface-active copper sites (D) (Table S2)
 156 were calculated as: (Eqs. 3, 4)

157
$$S = 2 \times Y \times N_{\text{av}} / (X \times M_{\text{Cu}} \times 1.4 \times 10^{19}) \quad (3)$$

158
$$D = (2 \times Y/X) \times 100 \quad (4)$$

159 where N_{av} = Avogadro's number, M_{Cu} = the relative atomic mass, and 1.4×10^{19} represents the
160 number of copper atoms per square meter.

161 **DFT Calculations**

162 Quantum-ATK along with VESTA and Virtual NanoLab Version 2019.3 software was
163 employed for the electronic properties simulations of CuO, MgO, Fe₃O₄, CuO/MgO, and
164 CuO/MgO/Fe₃O₄. Density functional theory (DFT) was used for the electronic property's
165 simulations and the detail procedure was given as text S6.

166 **Results and Discussion**

167 **PMS Activation by Different Catalysts**

168 The catalytic performance of CuOMgO/Fe₃O₄ along with different controlled catalysts i.e. CuO,
169 Fe₃O₄, MgO, MgO/Fe₃O₄, CuO/Fe₃O₄ and CuOMgO is evaluated during the degradation of 4-
170 CP using PMS activated system (Figure 1A and and Figure S1). As shown, the catalytic
171 performance of various controlled catalysts i.e. MgO, Fe₃O₄, MgO/Fe₃O₄ and CuO or a
172 physical mixture of CuO plus Fe₃O₄ is very poor as revealed from less than 10-30% of 4-CP
173 removal. In the case of bimetallic CuO/Fe₃O₄ catalyst, the removal efficiency was slightly
174 improved to 42%. More interestingly, the degradation of 4-CP reached to 100% with the
175 degradation rate of 0.14-0.16 min⁻¹ for CuOMgO or CuOMgO/Fe₃O₄ catalysts, 16 to 50 times
176 higher than CuO/Fe₃O₄ (0.01 min⁻¹), CuO (0.008 min⁻¹) or Fe₃O₄ (0.003 min⁻¹). Additionally,
177 the negligible removal efficiency while using CuOMgO/Fe₃O₄ as adsorbent or homogeneous
178 activation (~100 times to the leached amount of Cu²⁺ and Fe²⁺) demonstrated the important
179 role of heterogeneous PMS activation. Furthermore, the very poor performance of various
180 catalysts i.e. Fe₃O₄, CuO, CuO/Fe₃O₄ or MgO/Fe₃O₄ clearly revealed that the enhanced
181 catalytic activity of CuOMgO or CuOMgO/Fe₃O₄ was resulted from the increase reactivity of
182 only copper after the incorporation of MgO whereas Fe₃O₄ can only function as support

183 material, offering the easy recovery of catalyst during reusing. By considering these interesting
184 results, it was necessary to explore the role of MgO more deeply. We therefore, replaced MgO
185 in CuO/Fe₃O₄ catalyst with the oxides of other divalent metals. As shown in Figure S2, the
186 catalytic activity was gradually decreased after replacing MgO with CaO or BaO. This decrease
187 might be related to the large ionic size of Ca²⁺ or Ba²⁺, influencing the crystal structure of
188 catalyst. As shown (Figure S3 and Table S3), the XRD peaks corresponded to the crystal planes
189 of pure CuO shifted significantly toward the low 2θ after replacing MgO with CaO or BaO.
190 These results thus suggested that the changes in the catalytic activity of CuO in CuO/Fe₃O₄
191 catalyst is related to the structural changes. The structural changes in CuO might be more
192 interesting as the incorporation of Zn²⁺ with ionic radii close to Mg²⁺ (Mg²⁺=0.065 nm, Zn²⁺=
193 0.074 nm), also leads to good catalytic activity, showing positive influence the activity of CuO.
194 We further considered the PMS decomposition efficiency to evaluate the role of MgO in
195 CuOMgO/Fe₃O₄. As shown in Figure 1B, both Fe₃O₄ and MgO/Fe₃O₄ were involved in less
196 than 10% PMS decomposition. In contrast, the PMS decomposition gradually increased from
197 CuO to CuO/Fe₃O₄ and finally reached 100% in the case of CuOMgO and CuOMgO/Fe₃O₄.
198 These results are in accordance with the catalytic activity order and support strongly that the
199 enhanced catalytic activity was related to the changes in the catalytic activities of copper after
200 the incorporation of MgO. By considering these interesting results, we choose the influence of
201 MgO on the reactivity of other redox metals such as Co and Mn. As shown in Figure 1C and
202 Figure S1, the catalyst such as Co₃O₄MgO/Fe₃O₄ showed significant improvement with 4-CP
203 degradation rate (k=0.027 min⁻¹), higher than Co₃O₄/Fe₃O₄ (k=0.013 min⁻¹) or Co₃O₄ (k=0.009
204 min⁻¹). A similar pattern of increase was observed for MnO₂MgO/Fe₃O₄ (k=0.022 min⁻¹),
205 highlighting the positive influence of MgO on the catalytic activities of redox metals. More
206 interestingly, the remarkable improvement in the catalytic activity of CuOMgO/Fe₃O₄
207 emphasized maximum influence of MgO on the reactivity of studied redox metals. Additionally,

208 the influence of support material (Figure 1C and Figure S1) indicate the highest degradation
209 rate ($k=0.19 \text{ min}^{-1}$) for CuOMgO/SiO₂, followed by CuOMgO/Fe₃O₄ ($k=0.16 \text{ min}^{-1}$) and
210 CuOMgO/Al₂O₃ ($k=0.028 \text{ min}^{-1}$). The easy recovery owing to the magnetic property gives
211 extra advantage to CuOMgO/Fe₃O₄ for real application and thus was chosen for detail studies.

212 **Changes in the Redox Properties of Copper after the Incorporating MgO**

213 The above results clearly revealed that the incorporated MgO play important role to modify the
214 activity of different Cu-supported catalysts. We believed that this improvement is originated
215 from the significant changes in the catalytic properties of CuO. First, the structural changes
216 observed after replacing MgO with the oxides of other divalent metals (Figure S3 and Table
217 S3) highlighted the structure-activity relationship of CuO. More precisely, the changes in the
218 crystal structural of CuO might be important as the incorporation of ZnO in CuO/Fe₃O₄ catalyst
219 with ionic radii close to Mg²⁺ and Cu²⁺ (Mg²⁺=0.72 Å, Zn²⁺= 0.74 Å and Cu²⁺= 0.73 Å), also
220 leads to good catalytic activity. Additionally, the incorporation of MgO was accounted to
221 increase the surface area (Table S2) and thus correspondingly increase the fine dispersion of
222 active sites. In order to correlate the enhanced catalytic with surface area, normalized rate
223 constants were calculated (Figure S4). The results revealed that the increase of surface area
224 after the incorporation of MgO might not be very important in the enhanced activity of copper
225 due the big difference in the normalized rate constants of CuOMgO/Fe₃O₄ ($0.02 \text{ L m}^{-2} \text{ min}^{-1}$)
226 and CuO/Fe₃O₄ ($0.004 \text{ L m}^{-2} \text{ min}^{-1}$). In contrast, these results highlighted that the enhanced
227 activity was related to the increased reactivity of copper as active site after the incorporation
228 of MgO.

229 Analyzing solid CuO/Fe₃O₄ and CuOMgO/Fe₃O₄ catalysts on XPS, H₂-TPR and Raman
230 spectroscopy gave us a solid evidence for the enhanced catalytic activity after the incorporation
231 of MgO. For example as shown in Figure S5, the incorporation of MgO in CuOMgO/Fe₃O₄

232 shifted the Cu 2p core spectra toward the high binding energy (B.E 0.88 V), facilitating the
233 generation of Cu ions in highly electron deficient state, most probably be Cu^{3+} species, which
234 offered the highest redox potential for PMS activation (E_0 $\text{Cu}^{(\text{III})}/\text{Cu}^{(\text{II})}$ 2.3 V vs $\text{HSO}_5^-/\bullet\text{SO}_4^-$
235 1.8 V).⁸⁻¹⁰ The H_2 -TPR analysis (Figure S6) showed two-stage desorption processes for the
236 $\text{CuOMgO}/\text{Fe}_3\text{O}_4$: one reduction peak at 157 °C followed by another one at 254 °C, which were
237 attributed to the reductions of Cu species ($\text{Cu}^{3+} \rightarrow \text{Cu}^{2+}$ and $\text{Cu}^{2+} \rightarrow \text{Cu}^{+1}$).^{38,40} In contrast, the
238 intense reduction peaks of the $\text{CuO}/\text{Fe}_3\text{O}_4$ were shifted to much higher temperatures (218 and
239 345 °C), indicating that the Cu species in the $\text{CuO}/\text{Fe}_3\text{O}_4$ catalyst were less electron deficient
240 as compared to $\text{CuOMgO}/\text{Fe}_3\text{O}_4$. Moreover, calculated from the chemical adsorption volume
241 of H_2 , the % CuO_x dispersion and exposed CuO_x active surface area was 16.62% and 112.40
242 m^2/g , respectively, for the $\text{CuOMgO}/\text{Fe}_3\text{O}_4$, both of which were obviously higher than
243 $\text{CuO}@/\text{Fe}_3\text{O}_4$ (12.53% and 84.79 m^2/g , respectively), (Table S2). Raman spectroscopy was
244 applied to confirm the evidence of XPS and H_2 -TPR analysis. As shown in Figure 1D, the
245 characteristics Raman peaks corresponded to Fe_3O_4 and CuO were broader for both $\text{CuO}/\text{Fe}_3\text{O}_4$
246 and $\text{CuOMgO}/\text{Fe}_3\text{O}_4$ catalysts. However, the shifting in the latter case was more obvious,
247 indicating the abundant lattice defects and more reactive active sites.⁴¹ More interestingly, the
248 marker peak of Cu^{3+} state at 603 cm^{-1} as reported in the characteristic Raman spectrum of
249 NaCuO_2 was only observed in $\text{CuOMgO}/\text{Fe}_3\text{O}_4$ catalyst.⁴² This result give us another solid
250 evidence for the existence of Cu^{3+} state, and thus confirmed the findings of XPS and H_2 -TPR
251 analysis.

252 To clarify the role of MgO in the generation of Cu^{3+} state, we performed a series of DFT
253 calculations to simulate the partial density of states (PDOS), band structure simulation and
254 Bader charge transfer analysis of CuO , Fe_3O_4 , CuOMgO and $\text{CuOMgO}/\text{Fe}_3\text{O}_4$. The detail
255 simulation procedure is given in the supporting information as Text S6. First, partial density of
256 states (PDOS) simulation were applied to investigate the changes in the electronic states, after

257 the incorporation of MgO (Figure S7). In the case of CuO/Fe₃O₄ system (Figure S7 A), Cu has
258 the highest density of states in the valence band (VB) while the conduction band (CB) is equally
259 contributed by the anti-bonding orbitals of O, Fe, and Cu atoms. On the other hand, the density
260 of states of Cu in the VB of CuOMgO/Fe₃O₄ is comparatively reduced while its density is
261 increased in the CB (Figure 7S B). In addition, the Fermi energy level of CuO/Fe₃O₄ has also
262 been increased from -5.33 to -5.37 eV, upon MgO incorporation. In order to further clarify this
263 effect, the density of states for valence and conduction bands of CuOMgO/Fe₃O₄ were plotted
264 separately (Figure S8). Comprehensive analysis of Figure S8 and the spin-up down PDOS
265 spectra of CuOMgO/Fe₃O₄ (Figures S9), clearly suggested that the density of states of Cu in
266 the CB of CuOMgO/Fe₃O₄ increases, due to the oxidation of some of the Cu atoms i.e., from
267 Cu²⁺ to Cu³⁺. Furthermore, the comparative analysis of band structure of CuO/Fe₃O₄ and
268 CuOMgO/Fe₃O₄ (Figures S10-S12) let us to conclude that MgO has produced an extra band
269 within the bandgap of parent CuO/Fe₃O₄, responsible for the bandgap reduction and trapping
270 centre of extra charge (Cu³⁺). This band arises from the anti-bonding orbital of Mg in the spin-
271 up state only, while it is fully hybridized with anti-bonding orbitals of Fe, Cu and O atoms, as
272 can be seen from Figure S11 and S12. Therefore, the changes in density of state of VB and CB
273 after the incorporation of MgO is responsible for the generation of Cu³⁺ state as also evident
274 from Bader charge analysis. The results of Figure S13 and Table S4, suggested that Cu has +2
275 charge in CuO while its valency increases from Cu²⁺ to Cu³⁺, upon interaction of MgO either
276 in the case of CuOMgO or CuOMgO/Fe₃O₄. For example, Cu donates about ~1.54 electrons to
277 O which form Cu²⁺ state in the case of CuO/Fe₃O₄ (Figure S13 A). On the other hand, Cu
278 donates about ~2.65 electrons (equivalent to Cu³⁺ state) and thus enhanced the performance of
279 both CuO/MgO and CuOMgO/Fe₃O₄ heterostructure due to the presence of Cu in high
280 oxidation state.

281 **Identification of Reactive Oxygen Species**

282 Sulfate ($\text{SO}_4^{\bullet-}$) and hydroxyl ($\bullet\text{OH}$) radicals have been reported as the dominant reactive
283 species in PMS activated systems.²¹⁻²⁴ Firstly, tertiary butyl alcohol (TBA) and ethanol were
284 applied in excess amount (1000 fold) as selective radical scavengers for $\bullet\text{OH}$ and $\text{SO}_4^{\bullet-}$ radicals
285 because of their dissimilar second-order rate constants. For example, TBA react quickly with
286 $\bullet\text{OH}$ radicals ($k_2(\text{TBA}, \bullet\text{OH}) = 3.6\text{--}7.6 \times 10^9 \text{ M}^{-1}\text{s}^{-1}$), over 1000 fold faster than $\text{SO}_4^{\bullet-}$ ($k_2(\text{TBA},$
287 $\text{SO}_4^{\bullet-} = 4\text{--}9.1 \times 10^5 \text{ M}^{-1}\text{s}^{-1}$). Similarly, ethanol react both $\bullet\text{OH}$ and $\text{SO}_4^{\bullet-}$ radicals nearly with
288 the same rate i.e. $k_2(\text{ethanol}, \bullet\text{OH}) = 1.1\text{--}2.8 \times 10^9 \text{ M}^{-1}\text{s}^{-1}$) and $k_2(\text{ethanol}, \text{SO}_4^{\bullet-} = 1.6\text{--}7.8 \times$
289 $10^7 \text{ M}^{-1}\text{s}^{-1}$) and thus can used to trap both radicals.⁷ As shown in Figure 2A and Figure S14, the
290 inhibitory effect of both these scavengers were negligible for $\text{CuOMgO}/\text{Fe}_3\text{O}_4 + \text{PMS}$ system as
291 k_{obs} only changes from 0.162 min^{-1} to 0.150 min^{-1} or 0.152 min^{-1} after applying excess amount
292 of ethanol or TBA. In contrast, the degradation rate of 4-CP in the $\text{CuO}/\text{Fe}_3\text{O}_4 + \text{PMS}$ system
293 decreased from 0.01 min^{-1} to 0.008 min^{-1} in the presence of ethanol and to 0.004 min^{-1} in the
294 presence of TBA (Figure S15). Similarly, for the $\text{CuO} + \text{PMS}$ system, the degradation rate of 4-
295 CP was also influenced by both ethanol and TBA (Figure S16). These results thus highlighted
296 that the incorporated MgO as $\text{CuOMgO}/\text{Fe}_3\text{O}_4$ play important role to switch the degradation
297 pathway from radical to non-radical process. To further confirm these results, we performed
298 the scavenging studies on $\text{CuOCaO}/\text{Fe}_3\text{O}_4$ and $\text{CuOZnO}/\text{Fe}_3\text{O}_4$ catalysts where MgO was
299 replaced with the oxides of other divalent metals. As shown in Figure S17, the degradation of
300 4-CP was not inhibited in both $\text{CuOCaO}/\text{Fe}_3\text{O}_4 + \text{PMS}$ and $\text{CuOZnO}/\text{Fe}_3\text{O}_4 + \text{PMS}$ system after
301 applying excess amount of radical scavengers and thus indicated the presence of reactive
302 species similar like $\text{CuOMgO}/\text{Fe}_3\text{O}_4 + \text{PMS}$ system. In contrast, the degradation was inhibited
303 significantly in the case of $\text{CuOCO}_3/\text{Fe}_3\text{O}_4 + \text{PMS}$ system where MgO was replaced with the
304 oxide of transition metals. These results thus strongly verify the major role of MgO to change
305 the reaction mechanism from radical to non-radical.

306 Moreover, we applied sodium azide (NaN_3) at different concentrations (inset of Figure 2A and
307 Figure S18) to quench the singlet oxygen ($k_2 \text{}^1\text{O}_2 = 1 \times 10^9 \text{ M}^{-1}\text{s}^{-1}$).²⁶⁻³⁰ As shown, the
308 degradation of 4-CP was almost suspended in CuOMgO/ Fe_3O_4 +PMS system in the presence
309 of 50-100 mM NaN_3 . For example, almost 90% inhibition with a decrease in the degradation
310 rate from the initial 0.16 min^{-1} to 0.006 min^{-1} was noted after adding 100 mM NaN_3 . In contrast,
311 the degradation rate of 4-CP in the presence of CuO/ Fe_3O_4 +PMS was barely affected (Figure
312 S19). These results thus suggested the dominant role of $\text{}^1\text{O}_2$ in CuOMgO/ Fe_3O_4 +PMS system.
313 To validate the leading role of $\text{}^1\text{O}_2$, the degradation of FFA as $\text{}^1\text{O}_2$ -indicator was performed
314 (Figure 2B and Figure S20).⁴³ As shown, the removal of FFA through adsorption or PMS alone
315 was negligible, however the removal was more rapid when the catalyst and PMS were applied
316 together and almost all FFA (0.1-10 mM) was completely removed in different reaction time.
317 The first order degradation rate constant of FFA, calculated at 0.1 mM was 0.3085 min^{-1} , which
318 was far higher than that of 4-CP (0.16 min^{-1}). Moreover, the calculated amount of $\text{}^1\text{O}_2$ from the
319 degradation of FFA, using the equation of $[\text{}^1\text{O}_2] = k_{\text{obs}}/\text{FFA}$, was $1.848 \times 10^{-4} \text{ M}$ (at 10.0 mM
320 FFA) (Figure S20), which was much higher than MnO_2 /PDS system ($1.65 \times 10^{-11} \text{ M}$ at 0.3
321 mM FFA)²⁶ and typical $\text{}^1\text{O}_2$ -mediated RB light irradiated system ($0.05 \times 10^{-11} \text{ M}$ at 0.27 mM
322 FFA).³⁵ To further confirmed the presence of $\text{}^1\text{O}_2$ as dominant reactive species, the degradation
323 of 4-CP was conducted in D_2O . As shown in Figure S21, the kinetic degradation of 4-CP was
324 significantly increased after exchanging H_2O with D_2O . This improvement was related to the
325 enhanced stability of $\text{}^1\text{O}_2$ (10 times) in D_2O and thus gives strong evidence for the generation
326 of singlet oxygen.⁴³ To endorse the results of the chemical scavengers, electron paramagnetic
327 resonance was also applied. The typical three-line spectrum (1: 1: 1) with TEMP (Figure 2C),
328 confirmed the presence of $\text{}^1\text{O}_2$ in the CuOMgO/ Fe_3O_4 +PMS system. In addition, the intensities
329 of the three-line spectra decreased after adding NaN_3 (5 mM) or FFA (0.1 mM) due to the
330 scavenging of singlet oxygen. In contrast, no signals were observed for $\bullet\text{OH}$ or $\text{SO}_4\bullet$ after

331 adding DMPO (Figure S22) in water. These results thus verified that the degradation process
332 in CuOMgO/Fe₃O₄+PMS system was dominantly controlled by ¹O₂ oxidation process.

333 **Interactions between Catalyst and PMS**

334 Previously we compared the decomposition of PMS between Fe₃O₄, MgO/Fe₃O₄, CuOMgO
335 and CuOMgO/Fe₃O₄ to demonstrate the reactivity originated from CuO rather than from Fe₃O₄
336 (Figure 2B). Herein, we conducted additional experiments to see how the decomposition of
337 PMS was influenced by the addition of 4-CP to further investigate the interactions between
338 catalysts and PMS (Figure 1B and Figure S23). As shown, the presence of both catalysts
339 without organic decomposed PMS to significant extent. However, the decomposition of PMS
340 was 13 times faster for CuOMgO/Fe₃O₄ as compared to CuO/Fe₃O₄. The faster PMS
341 decomposition was related to Cu³⁺ state, as revealed above, offering thermodynamically
342 feasible sites to accept electron from PMS (E_0 Cu^(III)/Cu^(II) 2.3 V vs. E^0 HSO₅⁻/SO₄²⁻ 1.81 V).
343 This was further evidenced from the gradual increase in the reduction peaks of CuOMgO/Fe₃O₄
344 after applying increasing amount of PMS (Figure 2D), and thus highlighted the reverse
345 phenomena from the early reports.^{22,44-45} Additionally, the decrease of PMS decomposition
346 after 4-CP addition (Figure S23) ruled out the mediator role of catalyst as proposed in the early
347 reports,^{22,44-45} through which the direct electron transfer between organic contaminants and
348 PMS was considered as the dominant process. Additionally, the improved charge transfer
349 ability of CuOMgO/Fe₃O₄ by EIS and CV studies (Figure S24) further demonstrated that Cu³⁺
350 state could accept electron more quickly from PMS, and thus induce faster PMS decomposition.

351 Another property is the type of complexation (inner-sphere vs. outer-sphere) of PMS to decide
352 the nature of dominant mechanism.^{7,21} Therefore, we studied the complexation behavior of
353 PMS at the surface of CuOMgO/Fe₃O₄ and CuO/Fe₃O₄ at increasing ionic strength (taken as
354 1–100 mM NaClO₄). In the case of CuOMgO/Fe₃O₄, the degradation of 4-CP was significantly

355 influenced at increasing ionic strength (Figure S25). This relationship revealed that the
356 interaction between the CuOMgO/Fe₃O₄ and PMS occurred through the outer-sphere surface
357 complexation because the increasing ionic strength inhibited the electrostatic interactions
358 between the PMS molecules and catalyst particles. In contrast, the degradation of 4-CP was
359 not influenced for CuO/Fe₃O₄ at increasing ionic strength due to presence of the inner-sphere
360 complexation (covalent or ionic bonding) between the catalyst particles and PMS molecules
361 (Figure S26).^{7,21} ATR-FTIR spectra was further applied to visualize the inner-sphere
362 complexation of S–O bond coming from the PMS in the range of 1249–1060 cm⁻¹.²¹ As shown
363 (Figure 3A), we obtained the evidence of bonding PMS at the surface of catalyst in the IR range
364 of 1101–1097 cm⁻¹ for radical dominant systems (CuO/PMS or CuO/Fe₃O₄/PMS). In contrast,
365 the absence of IR peaks in the above range confirmed the lack of inner-sphere complexation
366 between PMS and CuOMgO/Fe₃O₄ catalyst.

367 The changes in the complexation was interesting to decide the difference between radical and
368 non-radical oxidation process. Surface hydroxyl group is documented in many recent
369 publication and is believed to play important role in the catalytic activity of catalysts.⁴⁶⁻⁴⁹
370 Therefore, we expected that the changes in the surface hydroxyl groups after the incorporation
371 of MgO might be important to change the PMS complexation from inner sphere to outer sphere.
372 Therefore, we compared the proportion of surface hydroxyl groups on CuOMgO/Fe₃O₄,
373 CuO/Fe₃O₄ and CuO and Fe₃O₄ catalysts (Figure S27). Based on the XPS peak area (Figure
374 S27), the proportion of terminal-OH, bridging-OH and oxides (50: 36: 14) at the surface of
375 CuOMgO/Fe₃O₄ was much higher than the dominant radical based catalysts i.e. CuO/Fe₃O₄,
376 CuO and Fe₃O₄.⁴⁶ Additionally, the XPS results were further verified through FTIR analysis
377 (Figure S28). As shown, the incorporation of MgO as CuOMgO or CuOMgO/Fe₃O₄ visibly
378 increased the intensity of peak corresponded to terminal-OH and bridging-OH groups.^{50,51}
379 Even though, all oxides are hydroxylated due to the chemisorption of water, however, the

380 increase of hydroxyl groups (terminal-OH and bridging-OH) at the surface of CuOMgO/Fe₃O₄
381 after the incorporation of MgO is not surprising because MgO is strongly basic with high
382 isoelectric point of 11.80.⁵² Thus it is inferred that the densely OH covered surface of
383 CuOMgO/Fe₃O₄ might provide strong binding sites for PMS through H-bonding,^{50,51} leading
384 to strong electrostatic interactions and changes the complexation behaviour of PMS from inner
385 sphere to outer sphere. Furthermore, the DFT calculations also clarified that the OH groups on
386 the surface of CuOMgO/Fe₃O₄ catalyst are more strongly bonded (bond length 1.99 Å) as
387 compared to CuO/Fe₃O₄ (2.28 Å), showing adsorption energy (-1563.27 kcal/mol Table S5),
388 eight times higher (202.01 kcal/mol) than CuO/Fe₃O₄ (Figure S29 and S30). The shorter bond
389 length and high adsorption energy in the case of CuOMgO/Fe₃O₄ catalyst might related to the
390 existence of strong H-bonding between the surface OH groups,^{51,52} and thus supporting
391 indirectly the existence of strong electrostatic interactions between PMS and catalyst particle.
392 Since, HPO₄⁻ offer strong affinity to replace the surface OH groups of catalyst and interact
393 directly the active sites through inner sphere complexation.⁵³ Therefore, it is expected that the
394 application of H₂PO₄ during 4-CP degradation would disturb the H-bonding interactions of
395 PMS and surface OH groups. As shown (Figure S31), the significant influence on 4-CP
396 degradation in the presence of H₂PO₄ is related to the unavailability of surface hydroxyl groups
397 to interact PMS and thus gives direct evidence for the importance of surface OH groups. These
398 results thus gives us enough evidences to support the switching of PMS complexation from
399 inner-sphere to outer-sphere was related to the presence of extensive surface hydroxyl groups
400 after MgO incorporation, responsible for generating different reactive species.

401 **Proposed Mechanism for the Generation of ¹O₂**

402 The generation of singlet oxygen can be achieved by many pathways including the reaction
403 between PMS/PDS and kenotic groups in carbonaceous materials,²⁵ or through the photo-

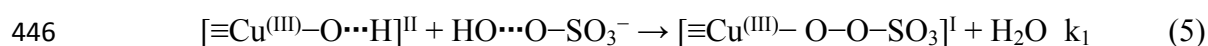
404 excitation of oxygen molecules.⁵⁴ In this study, we proposed that superoxides ($\bullet\text{O}_2^-$) might
405 function as precursors for the generation of singlet oxygen.²⁶ BQ ($k_2 = 2.9 \times 10^9 \text{ M}^{-1}\text{s}^{-1}$) and
406 bicarbonate ($k_2 = 5 \times 10^8 \text{ M}^{-1} \text{ s}^{-1}$) as scavenger of $\bullet\text{O}_2^-$ were applied (Figure S32).²⁶ As shown,
407 the degradation of 4-CP was decreased from 100% to 78% or to 12% after adding 1 and 2 mM
408 BQ, respectively. Besides BQ, sodium bicarbonate as the scavenger of $\bullet\text{O}_2^-$ also influenced the
409 degradation 4-CP.

410 Since, both BQ ($\text{OH}\bullet$, $k_2 = 1.2 \times 10^9 \text{ M}^{-1}\text{s}^{-1}$) and bicarbonate ($\bullet\text{OH}$, $k_2 = 3 \times 10^8 \text{ M}^{-1} \text{ s}^{-1}$) can
411 also react other free radicals, therefore the presence of $\bullet\text{O}_2^-$ was further confirmed from the
412 EPR analysis. As shown in Figure 3B, the characteristic signals of DMPO- O_2 adduct appeared
413 only in ethanol due to the extra stability of $\bullet\text{O}_2^-$ in organic solvent. The absence of DMPO- O_2
414 adduct in water (Figure S22), might be related to the transformation of $\bullet\text{O}_2^-$ to singlet oxygen.
415 Additionally, the generated superoxide is expected to produce H_2O_2 , during the generation of
416 singlet oxygen.⁵⁵ Molybdate salt rapidly reacts with H_2O_2 to produce peroxymolybdate
417 complex, which can be easily detected in the UV spectra.⁵⁶ As shown in Figure S33, the
418 adsorption for peroxymolybdate complex gradually increased in the first 10 minutes and then
419 was hardly detected after extending the reaction time. These results thus confirmed the
420 intermediate role of $\text{O}_2^{\bullet-}$ during the generation of singlet oxygen.

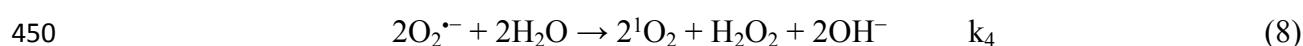
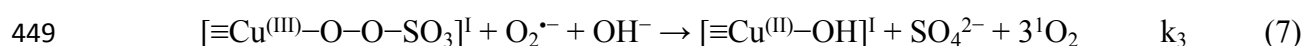
421 XPS analysis were performed for the CuO, CuO/ Fe_3O_4 and CuOMgO/ Fe_3O_4 catalysts to
422 investigate the changes in the oxidation state of Cu after the incorporation of MgO (Figure S34).
423 From the deconvoluted peaks of Cu $2p_{3/2}$, the peaks for CuO and CuO/ Fe_3O_4 at the binding
424 energy (B.E) of 932.03–934.04 eV were assigned to +2 oxidation state of copper (Figure S34
425 A,B).^{9–10,57} In contrast, the Cu $2p_{3/2}$ spectra for CuOMgO/ Fe_3O_4 catalyst shifted toward higher
426 B.E side i.e. 0.84 eV from CuO and 1.06 eV from CuO/ Fe_3O_4 (Figure S34 C). This shifting
427 clearly demonstrated that the Cu^{2+} cation in CuOMgO/ Fe_3O_4 catalyst is more electron deficient

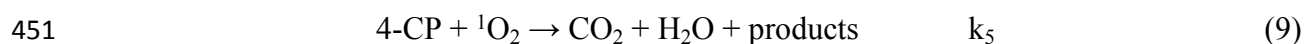
428 and thus suggested the oxidation of Cu^{2+} to Cu^{3+} species.⁵⁸ After reaction, the proportion of
 429 proposed Cu^{3+} ions decreased from 48% to 37% and that of Cu^{2+} ions increased from 52% to
 430 63% (Figure S34 C,D). This change is probably attributed to the electron transfer from PMS to
 431 $\text{Cu}^{(\text{III})}$, during the generation of singlet oxygen.

432 Therefore, together with all characterizations on the Cu species in $\text{CuOMgO/Fe}_3\text{O}_4$, a reaction
 433 pathway based on $\text{O}_2^{\bullet-}$ was proposed for the generation of $^1\text{O}_2$ (Eqs. 5–9). At first, the
 434 incorporation of MgO with extensive hydroxyl groups facilitating the generation of Cu–OH
 435 complex, a critical step for PMS activation. The high valent electron deficient copper $[\equiv\text{Cu}^{(\text{III})}-$
 436 $\text{OH}]^{\text{II}}$ reacts with PMS at the surface of $\text{CuOMgO/Fe}_3\text{O}_4$ and generates a metastable copper
 437 intermediate $[\equiv\text{Cu}^{(\text{III})}-\text{O}-\text{O}-\text{SO}_3]^{\text{I}}$ through outer-sphere complexation (Eq.5). Afterwards, the
 438 electron deficient center of copper produce $\text{O}_2^{\bullet-}$ after accepting electron from another PMS
 439 (HSO_5^-) molecule and thus breaks the coordination bond of metastable $[\equiv\text{Cu}^{(\text{III})}-\text{O}-\text{O}-\text{SO}_3]^{\text{I}}$
 440 intermediate (Eq. 6). Later, $^1\text{O}_2$ is generated from the direct oxidation of $\text{O}_2^{\bullet-}$ by the $\equiv\text{Cu}^{(\text{III})}$,
 441 which is thermodynamically feasible ($E_0 \text{ Cu}^{(\text{III})}/\text{Cu}^{(\text{II})}$ 2.3 V vs. $E_0 \text{ O}_2^{\bullet-}/^1\text{O}_2$ -0.34 V) or from
 442 recombination of two superoxide anions radicals (Eqs. 7–8). This activation mechanism is
 443 similar to Mn–Fe oxides induced PMS/PDS activation,^{26,32} and the ultimate electron transfer
 444 from PMS molecule to electron deficient $\equiv\text{Cu}^{(\text{III})}$ center endorsed the generation of superoxide
 445 and then singlet oxygen.



448 (6)





452 **Kinetic Study**

453 The kinetics for the above mechanism were established after changing the concentration of
454 PMS and catalyst dosage (Figure S35 and Figure S36). The study demonstrated that the
455 degradation of 4-CP increased at higher concentrations of PMS or catalyst dosages. The
456 degradation rate constant (k_{obs}) at a given PMS concentration and CuOMgO/Fe₃O₄ amount was
457 calculated after applying pseudo first-order kinetic rate equation. Then the curve fitting
458 between $\ln[k_{\text{obs}}]$ vs. $\ln[\text{PMS}]_0$ or $\ln[\text{CuOMgO/Fe}_3\text{O}_4]_0$ was established (inset, Figure S36). A
459 good linear correlation for $\ln[k_{\text{obs}}]$ vs. $\ln[\text{PMS}]_0$ (R^2 0.98) and $\ln[k_{\text{obs}}]$ vs. $[\text{CuOMgO/Fe}_3\text{O}_4]_0$
460 (R^2 0.94) was established with slopes of 1.107 and 0.89 respectively, suggesting that the kinetic
461 orders (n) of both process were close to 1. The first order of $[\text{PMS}]_0$ and $[\text{CuOMgO/Fe}_3\text{O}_4]_0$
462 could be assumed for reactions (Eqs. 5 and 6). Since Eq. 5 depend only on the
463 $[\text{CuOMgO/Fe}_3\text{O}_4]_0$ at an initial excess amount of $[\text{PMS}]_0$, and thus can be considered pseudo
464 first order reaction. On the other hand, the $[\text{CuOMgO/Fe}_3\text{O}_4]$ in Eq. 6 was irrelevant and the
465 reaction completely depend on the $[\text{PMS}]$. The kinetic studies recommended that the catalytic
466 process totally depend upon the generation of metastable copper intermediate (Eq.5), primarily
467 related to the adsorption and heterogeneous surface activation of PMS. Therefore, we applied
468 Langmuir-Hinshelwood (L-H) model,²⁶ to confirm the role of surface mediated
469 reactions/adsorption in CuOMgO/Fe₃O₄+PMS system (Figure S37-38). The well fitted L-H
470 model with excellent R^2 (0.97) after plotting $1/k_{\text{obs}}$ against $[\text{PMS}]_0$ (Figure S38 A), suggested
471 that the adsorption of PMS on the surface of CuOMgO/Fe₃O₄ to generate metastable
472 $[\equiv\text{Cu}^{\text{III}}-\text{O}-\text{O}-\text{SO}_3]^{\cdot}$ intermediates play important role in the in the enhanced catalytic activity
473 and generation of ${}^1\text{O}_2$.

474 **Advantages of Non-Radical Process**

475 The incorporation of redox-inactive MgO not only influences the reaction mechanism but also
476 changes some of the properties of heterogeneous catalyst such as stability. As disclosed above,
477 the leaching of both Cu^{2+} and Fe^{2+} ions was better controlled in $\text{CuOMgO/Fe}_3\text{O}_4$ as compared
478 to CuO or $\text{CuO/Fe}_3\text{O}_4$ (Table S2). This small leaching of metals ions also influenced the
479 stability of $\text{CuOMgO/Fe}_3\text{O}_4$. As shown in Figure 3C, the reused $\text{CuO/Fe}_3\text{O}_4$ catalyst induced a
480 continuous decrease in the removal of 4-CP after each cycle, whereas $\text{CuOMgO/Fe}_3\text{O}_4$
481 remained stable with approximately 100% removal in all reuse experiments. Furthermore, the
482 stability of the catalysts were also evaluated after comparing the structure changes before and
483 after the reaction. As shown in Figure S39 A, certain XRD peaks of $\text{CuO/Fe}_3\text{O}_4$ structure
484 completely disappeared after the 5th cycle, suggesting a poor structure stability during the
485 catalytic reaction. In contrast, the XRD spectra of $\text{CuOMgO/Fe}_3\text{O}_4$ remained the same even
486 after the 5th cycle, with only a small decrease in the intensity for certain side peaks (Figure S39
487 B). These results were also consistent with a much lower leaching of copper ions when MgO
488 was incorporated (Figure S40). Therefore, the incorporation of MgO not only enhanced the
489 reactivity of Cu in the $\text{CuOMgO/Fe}_3\text{O}_4$, but also induced better stability with a smaller leaching
490 amount and good reusability.

491 The performance of AOPs including PMS/PS system is strongly correlated with solution pH.¹⁰
492 As shown (Figure S41), the performance of $\text{CuOMgO/Fe}_3\text{O}_4$ +PMS system remained stable
493 (100% removal) in the initial pH 5.0-10, and then decreased to 80% when the initial pH was
494 raised to 12.0. These results are quite different from the activity of Rose Bengal (RB), a well-
495 known $^1\text{O}_2$ -mediation system,³⁵ when being applied under the same conditions (Figure S42).
496 Obviously these two system had so many differences, and three dominant factors can be
497 considered: 1) the buffer capacity of $\text{CuOMgO/Fe}_3\text{O}_4$, 2) the leaching of active component and
498 3) the interaction of catalyst, PMS and target compound.

499 Firstly, the removal trend of 4-CP under different initial pHs corresponded to the final pH of
500 solution (Figure S43). As shown, the eventual pH after the reaction remained stable at pH 9.0
501 ± 0.5 in the initial pHs ranged from 5.0 to 10.0. Thus the relatively constant performance ($k =$
502 $0.12 \sim 0.16 \text{ min}^{-1}$) in this pH range may be partly attributed to the buffer ability of
503 CuOMgO/Fe₃O₄. In the case of RB, this phenomena does not exist. Secondly, the lower activity
504 at pH 3.0 could be attributed to the leaching of heterogeneous catalysts (Figure S44 A), whereas
505 22 ppm Cu and 8 ppm Fe leaching was observed for CuOMgO/Fe₃O₄. On the other hand, the
506 low catalytic activity at pH 12.0 could be explained by the fact that the surface of the
507 CuOMgO/Fe₃O₄ becomes more negatively charged and consequently results in electrostatic
508 repulsion between the negatively charged CuOMgO/Fe₃O₄ ($\text{pH}_{\text{ZPC}} = 9.30$, Figure S45),
509 deprotonated 4-CP ($\text{p}K_{\text{a}} = 9.18$) and SO_5^{2-} ($\text{p}K_{\text{a}} = 9.41$). Furthermore, the active sites on the
510 surface of CuOMgO/Fe₃O₄ might also be passivated due the deposition of hydroxides layers
511 (Figure S46). In contrast, singlet oxygenated system (RB system) indicate significant
512 improvements in the degradation of 4-CP at high pH, because the above negative effects did
513 not emerge (Figure S42). This conclusion was further supported by the nonlinear relationship
514 between the degradation rate constants k and F factor calculated from Eq. 10,²⁶ (Figure S47),
515 which also suggested that the decrease of 4-CP degradation at high pH was resulted from
516 the surface electrostatic repulsion.

$$517 \quad F = k_w / [\text{H}^+] + k_a \quad (10)$$

518 Bromate (BrO_3^-) is one of the most alarming byproduct of AOPs, listed as possible human
519 carcinogen, and it is commonly generated in free radical AOPs.³⁶ Considering the threat level
520 of bromate, CuOMgO/Fe₃O₄+PMS system was evaluated for the generation of BrO_3^- after
521 reacting in brominated water (Figure S48). As shown, the generation of huge amount of BrO_3^-
522 in Co^{2+} /PMS system was accounted for the reaction of $\text{SO}_4^{\bullet-}$ radicals and bromide ions. In

523 contrast, no BrO_3^- was detected in CuOMgO/Fe₃O₄+PMS system which highlighted the
524 advantage of non-free radical process over free radical process.

525 Inorganic anions such as Cl^- and CO_3^{2-} are common background electrolytes in real wastewater.
526 Normally, their existence negatively influences the efficiency of radical-based advanced
527 oxidation processes. Both $\bullet\text{OH}$ and $\text{SO}_4\bullet$ radicals tend to be rapidly scavenged by halogens
528 ions with a high reaction rate constants ($k_{\text{SO}_4\bullet/\text{Cl}^-} = (3.2 \pm 0.2) \times 10^8 \text{ M}^{-1}\text{s}^{-1}$, $k_{\bullet\text{OH}/\text{Cl}^-} = 4.2 \times 10^9$
529 $\text{M}^{-1}\text{s}^{-1}$).^{24,59-60} Therefore, the influence of inorganic anions on the efficiency loss of the
530 CuOMgO/Fe₃O₄+PMS system was also investigated. Figure 3D depicts that the Cl^- , NO_3^- ,
531 SO_4^{2-} and CH_3COO^- anions demonstrated negligible influences on the degradation efficiency
532 of 4-CP. Due to the fact that $\bullet\text{OH}$ and $\text{SO}_4\bullet$ radicals were not produced, the small scavenging
533 of CO_3^{2-} and HCO_3^- (~10-15%) might be from the selective scavenging of $\bullet\text{O}_2^-$ anions (CO_3^{2-} ,
534 $k_2 = 5 \times 10^8 \text{ M}^{-1}\text{s}^{-1}$).²⁶ Additionally, humic acid (HA, a typical NOM), which is excessively
535 found in wastewater and is considered to be another free radical scavenger.⁷ The analysis
536 showed that HA decreased the degradation of 4-CP in the initial 20 minutes. However, the
537 scavenging effects became less important when the reaction time was extended to 40 minutes
538 (Figure S49). The decrease in the initial 20 minutes might be related to the adsorption of HA
539 on the surface of catalyst which could minimize the complexation of PMS to generate $^1\text{O}_2$. On
540 extending the reaction time, enough $^1\text{O}_2$ would be produced to proceed the reaction smoothly.

541 **Structure Activity Relationship and Degradation Pathway**

542 The degradation rate constants (k_{obs}) for 14 substituted phenols were calculated in
543 CuOMgO/Fe₃O₄+PMS system after applying pseudo-first order kinetics. The calculated k_{obs} in
544 CuOMgO/Fe₃O₄+PMS system were then compared with literature values obtained for similar
545 reactions in aqueous solution (Table S6).⁶⁰⁻⁶² Among the studied substituted phenols, 4-
546 MeCONH exhibited the maximum degradation rate with k_{obs} (0.168 min^{-1}), while 4-NO₂

547 phenol demonstrated the slowest oxidation with k_{obs} (0.037 min^{-1}). To describe the quantitative
 548 effect of substitution on the degradation rate of these phenols, the obtained k_{obs} values were
 549 changed to relative rates (k_{rel}) using 4-CP as the reference compound, as described in Eq 11.

$$550 \quad \log k_{\text{rel}} = \log \frac{k_{\text{obs}}}{k_{4\text{-CP}}} \quad (11)$$

551 Whereas k_{obs} is the pseudo-first-order degradation rate of different substituted phenols and $k_{4\text{-CP}}$
 552 is the observed rate constant of 4-CP. This type of normalization is very effective to give
 553 satisfactory structure-activity relationship in persulfate activation. Using this approach, we
 554 calculated $\log k_{\text{rel}}$ along with other substituent descriptor variables (i.e., Hammett constants σ ,
 555 σ^+ and σ^- and $E_{1/2}$) (Table S7). The obtained results were then compared to the substituent
 556 descriptor variables of Wang et al.,⁶⁰ using the degradation of similar substituted phenols in
 557 PMS activated system (Table S7). In the oxidative reactions of substituted phenols, Hammett
 558 constants (i.e. σ , σ^+ and σ^-) were mostly used to quantitatively correlate the electron donating
 559 (large negative value) or electron withdrawing (large positive value) properties of
 560 substituents.⁶¹⁻⁶³ Of the three Hammett constants (i.e. σ , σ^+ and σ^-), σ^+ give relatively good
 561 correlation (Figure 4 A and Figure S50 A,B) with linear regression as expressed in Eq. 12. The
 562 decrease in the oxidation rates of phenolic compounds with the increase of σ^+ (Table S7)
 563 suggested a typical electrophilic reaction between the reactive species ($^1\text{O}_2$) and substituted
 564 phenols.

$$565 \quad \text{Log} k_{\text{rel}} = 0.344 (\pm 0.103) - 0.752 (\pm 0.243) \times \sigma^+ \quad R^2 = 0.72 \quad (12)$$

566 On the other side, half-wave potential ($E_{1/2}$) reflects the ability of electron transfer as limiting
 567 step during the oxidation reactions and the values obtained are often used to construct
 568 quantitative structure-activity relationships (QSARs). Previously, the good linear relationship
 569 between the degradation rate of substituted phenol ($\log k_{\text{rel}}$) and $E_{1/2}$ was used to predict the rate
 570 limiting steps in CNT/PS system.⁶² In the case of CuOMgO/Fe₃O₄+PMS, a linear relationship

571 was established among the values of $E_{1/2}$ and $\log k_{rel}$ (Figure 4 B and Table S7). As shown, the
572 good linear relationship between $\log k_{rel}$ and $E_{1/2}$ highlighted one electron oxidation without
573 proton transfer as the rate limiting step during the oxidation of substituted phenols.

574 Meanwhile, in some cases $\log k_{rel}$ was not only correlated with the Hammett constant σ^+ , but
575 also showed good linear relationship with the pK_a values of organic contaminants,⁶⁴ which
576 indicated that not only the electron transfer but the proton transfer also contribute to oxidation,
577 as in the case of C-H bond cleavage by the non-selective radicals. In the system of
578 CuOMgO/Fe₃O₄+PMS however, there was no clear correlation between the $\log k_{rel}$ and pK_a
579 (Figure 4 C). This phenomenon together with the linear correlation of $\log k_{rel}$, σ^+ and $E_{1/2}$ thus
580 suggested the electron transfer mediated by ¹O₂ was the dominant oxidation process for organic
581 contaminants.

582 Additionally, kinetic isotopic effect (KIE) was also applied to reveal the electron transfer
583 process between the organic substrate and singlet oxygen. In general, $2 < \text{KIE} < 7$ can be used
584 to predict the C-H bond cleavage, which is typical for •OH radicals in hydrogen atom transfer
585 (HAT) process when attacking the aromatic ring. In contrast, the small KIE ($0.7 < \text{KIE} < 1.5$)
586 indicates that the hydrogen atom transfer is not the limiting step. In the system of
587 CuOMgO/Fe₃O₄+PMS, we compared the reaction rate constant with two substrate of phenol
588 and phenol-d₅ (Figure 4 D), and calculated KIE=1 (inset of Figure 4 D). This result once again
589 suggested that the oxidation of aromatic rings was dominantly through one electron transfer
590 process by ¹O₂, rather than HAT process as •OH mediated oxidations. This electron transfer
591 was highly consistent with our observation of the linear relationship of $\log k_{rel}$ and σ^+ but no
592 correlation on pK_a in QSARs study.

593 To sum up, the theoretical calculation based on the correlation of $\log k_{rel}$ with σ^+ and $E_{1/2}$
594 showed that the degradation of 4-CP began with the electron transfer from target compound to

595 $^1\text{O}_2$. Additionally, the high one electron standard reduction potential of $^1\text{O}_2/^{\bullet-}\text{O}_2$ (E_1° 0.79 V
596 NHE) than phenoxy/phenolate couple (E_1° 0.60 V NHE) also made this process
597 thermodynamically more feasible.⁶² Thus the electron transfer likely generated a transition
598 complex with a small amount of charge-transfer character (Figure S51, step 2), during which
599 the endoperoxide charged complex as result of cyclic-addition might act as highly unstable
600 intermediate. The good linear relationship and the kinetic isotopic effect (KIE) further
601 supported that this electron transfer mediated oxidation process by $^1\text{O}_2$ is the key step. Based
602 on GC-MS study, the identified products included chlorophenols, 1,4-benzoquinone and some
603 small open chain products (Table S8), while the additional products like di- or tri-
604 chlorophenols were not observed (Figure S51, step 1), which was further supported by the good
605 TOC removal efficiency (Table S2).

606 **Environmental Implications**

607 For the first time, we found that the incorporation of MgO not only enhanced the catalytic
608 properties but also modified the persulfate oxidation process from classical free radical
609 mechanism to non-radical mechanism. Normally in real water applications, heterogeneous
610 catalysts are loaded onto stable inorganic supports, which are commonly redox-inactive metal
611 oxides. Therefore, addressing the functional roles of these redox-inactive metal oxides in
612 regulating the environmental catalysts is of great importance. Secondly, we comprehensively
613 investigated the unique behaviour of this non-radical process from the view of kinetics,
614 interferences from water matrix, stability at broad pHs and the generation of toxic by-products
615 in complex water matrix. Interestingly, no toxic BrO_3^- was produced even in the presence of
616 spiked Br^- , suggesting another advantage of $^1\text{O}_2$ dominated process over classical radical ones.
617 The linear free energy relationships (LFERs) between the degradation rate constant of 14
618 substituted phenols and conventional descriptor variables (i.e. Hammett constant σ , σ^- , σ^+) in
619 quantitative structure activity relationship (QSARs) study not only offered insights into the

620 reaction mechanism that one electron oxidation is the dominant process by $^1\text{O}_2$, in which proton
621 transfer is not accompanied, but also offered clues to predict the reactivity of most common
622 phenol-substituted contaminants in non-radical PMS oxidation.

623 ASSOCIATED CONTENT

624 The supporting information i.e. Table S1-S8, Text S1-S7 and Figure S1-S52 were also given
625 in the supporting information. This information is available free of charge at
626 <http://www.pubs.acs.org>.

627 AUTHOR INFORMATION

628 Corresponding Author

629 *Phone: +8613476079416, E-mail address: zqchen@hust.edu.cn

630 **Notes:** The authors declare no competing financial interests.

631

632 ACKNOWLEDGMENT

633 This work was financially supported by the National Key R&D Program of China (No.
634 2018YFC1802302), the National Science Foundation of China (No. 21671072), the
635 Fundamental Research Funds for the Central Universities (No. 2019kfyRCPY058), and
636 Chutian Scholar Foundation from Hubei province. The authors also acknowledge the
637 Analytical and Testing Centre of Huazhong University of Science and Technology for SEM,
638 FTIR, XRD, XPS and elemental analyses.

639

640 References

- 641 1. Liu, X. W.; Zhang, T. Q.; Zhou, Y. C.; Fang, L.; Shao, Y. Degradation of atenolol by
642 UV/peroxymonosulfate: kinetics, effect of operational, parameters and mechanism.
643 *Chemosphere* **2013**, *93* (11), 2717–2724.

- 644 2. Yang, S. Y.; Wang, P.; Yang, X.; Shan, L.; Zhang, W. Y.; Shao, X. T.; Niu, R.
645 Degradation efficiencies of azo dye Acid Orange 7 by the interaction of heat, UV and
646 anions with common oxidants: Persulfate, peroxymonosulfate and hydrogen peroxide.
647 *J. Hazard. Mater.* **2010**, *179* (1–3), 552–558.
- 648 3. Chen, W. S.; Huang, C. P. Mineralization of aniline in aqueous solution by
649 electrochemical activation of persulfate. *Chemosphere* **2015**, *125*, 175–181.
- 650 4. Anipsitakis, G. P.; Dionysiou, D. D. Degradation of organic contaminants in water with
651 sulfate radicals generated by the conjunction of peroxymonosulfate with cobalt.
652 *Environ. Sci. Technol.* **2003**, *37* (20), 4790–4797.
- 653 5. Yang, Q. J.; Choi, H.; Dionysiou, D. D. Nanocrystalline cobalt oxide immobilized on
654 titanium dioxide nanoparticles for the heterogeneous activation of peroxymonosulfate.
655 *Appl. Catal., B* **2007**, *2*, 170–178.
- 656 6. Liu, H. Z.; Bruton, T. A.; Doyle, F. M.; Sedlak, D. L. In situ chemical oxidation of
657 contaminated groundwater by persulfate: Decomposition by Fe^(III) and Mn^(IV)
658 containing oxides and aquifer materials. *Environ. Sci. Technol.* **2014**, *48* (17),
659 10330–10336.
- 660 7. Zhang, T.; Zhu, H.; Croué, J. P. Production of sulfate radical from peroxymonosulfate
661 induced by a magnetically separable CuFe₂O₄ spinel in water: efficiency, stability, and
662 mechanism, *Environ. Sci. Technol.* **2013**, *47* (6) 2784-2791.
- 663 8. Li, Y.; Guo, L.; Huang, D.; Jawad, A.; Chen, Z.; Yang, J.; Liu, W.; Shen, Y.; Wang,
664 M.; Yin, G. Support-dependent active species formation for CuO catalysts: Leading to
665 efficient pollutant degradation in alkaline conditions. *J. Hazard. Mater.* **2017**, *328*, 56-
666 62.

- 667 9. Feng, Y.; Deli W.; Yu D.; Tong Z.; Kaimin S. Sulfate radical-mediated degradation of
668 sulfadiazine by CuFeO_2 rhombohedral crystal-catalyzed peroxymonosulfate:
669 synergistic effects and mechanisms. *Environ. Sci. Technol.* **2016**, *50*, 3119-3127.
- 670 10. Lei, Y.; Chen, C.S.; Tu, Y.J.; Ding, Y. Heterogeneous degradation of organic pollutants
671 by persulfate activated by $\text{CuO-Fe}_3\text{O}_4$: mechanism, stability and effects of pH and
672 bicarbonate ions, *Environ. Sci. Technol.* **2015**, *49*, 6838-6845.
- 673 11. Huang, G. X.; Wang, C. Y.; Yang, C. W.; Guo, P. C.; Yu, H. Q. Degradation of
674 bisphenol A by peroxymonosulfate catalytically activated with $\text{Mn}_{1.8}\text{Fe}_{1.2}\text{O}_4$
675 nanospheres: synergism between Mn and Fe. *Environ. Sci. Technol.* **2017**, *51* (21),
676 12611-12618.
- 677 12. Fang, G.D.; Liu, C.; Gao, J.; Dionysiou, D.D.; Zhou, D.M. Manipulation of persistent
678 free radicals in biochar to activate persulfate for contaminant degradation. *Environ. Sci.*
679 *Technol.* **2015**, *49* (9), 5645-5653.
- 680 13. Sun, H.Q.; Kwan, C.; Suvorova, A.; Ang, H.M.; Tade, M.O.; Wang, S.B. Catalytic
681 oxidation of organic pollutants on pristine and surface nitrogen-modified carbon
682 nanotubes with sulfate radicals. *Appl. Catal. B Environ.* **2014**, *154*, 134-141.
- 683 14. Chen, H.; Carroll, K.C. Metal-free catalysis of persulfate activation and organic-
684 pollutant degradation by nitrogen-doped graphene and aminated graphene. *Environ.*
685 *Pollut.* **2016**, *215*, 96-102.
- 686 15. Duan, X.G.; Su, C.; Zhou, L.; Sun, H.Q.; Suvorova, A.; Odedairo, T.; Zhu, Z.H.; Shao,
687 Z.P.; Wang, S.B. Surface controlled generation of reactive radicals from persulfate by
688 carbocatalysis on nanodiamonds. *Appl. Catal. B Environ.* **2016**, *194*, 7-15.
- 689 16. Lin, S. S.; Gurol, M. D. Catalytic decomposition of hydrogen peroxide on iron oxide:
690 Kinetics, mechanism, and implications. *Environ. Sci. Technol.* **1998**, *32* (10),
691 1417-1423.

- 692 17. Kwan, W. P.; Voelker, B. M. Decomposition of hydrogen peroxide and organic
693 compounds in the presence of dissolved iron and ferrihydrite. *Environ. Sci. Technol.*
694 **2002**, *36* (7), 1467–1476.
- 695 18. Furman, O. S.; Teel, A. L.; Watts, R. J. Mechanism of base activation of persulfate.
696 *Environ. Sci. Technol.* **2010**, *44* (16), 6423–6428.
- 697 19. Ji, Y.; Dong, C.; Kong, D.; Lu, J. New insights into atrazine degradation by cobalt
698 catalyzed peroxymonosulfate oxidation: kinetics, reaction products and transformation
699 mechanisms, *J. Hazard. Mater.* **2015**, *285*, 491-500.
- 700 20. Ross, A.B.; Neta, P. Rate constants for reactions of inorganic radicals in aqueous
701 solution. US department of commerce, national bureau of standards Washington D. C.
702 **1979**.
- 703 21. Zhang, T.; Chen, Y.; Wang, Y.; Le Roux, J.; Yang, Y.; Croué, J. P. Efficient
704 peroxydisulfate activation process not relying on sulphate radical generation for water
705 pollutant degradation. *Environ. Sci. Technol.* **2014**, *48* (10), 5868-5875.
- 706 22. Ahn, Y. Y.; Yun, E. T.; Seo, J. W.; Lee, C.; Kim, S. H.; Kim, J. H.; Lee, J. Activation
707 of peroxymonosulfate by surface-loaded noble metal nanoparticles for oxidative
708 degradation of organic compounds. *Environ. Sci. Technol.* **2016**, *50* (18), 10187-10197.
- 709 23. Duan, X.; Sun, H.; Shao, Z.; Wang, S. Nonradical reactions in environmental
710 remediation processes: Uncertainty and challenges. *App. Catal. B: Environ.* **2018**, *224*,
711 973-982.
- 712 24. Feng, Y.; Lee, P. H.; Wu, D.; Shih, K. Surface-bound sulfate radical-dominated
713 degradation of 1,4-dioxane by alumina-supported palladium (Pd/Al₂O₃) catalyzed
714 peroxymonosulfate. *Water Res.* **2017**, *120*, 12-21.

- 715 25. Cheng, X.; Hongguang G.; Yongli Z.; Xiao W.; Yang L. Non-photochemical
716 production of singlet oxygen via activation of persulfate by carbon nanotubes." *Water*
717 *Res.* **2017**, *113*, 80-88.
- 718 26. Zhu, S.; Li, X.; Kang, J.; Duan, X.; Wang, S. Persulfate activation on crystallographic
719 manganese oxides: Mechanism of singlet oxygen evolution for nonradical selective
720 degradation of aqueous contaminants. *Environ. Sci. Technol.* **2019**, *53*, (1), 307-315.
- 721 27. Tian, W.; Zhang, H.; Qian, Z.; Ouyang, T.; Sun, H.; Qin, J.; Tadé, M. O.; Wang, S.
722 Bread-making synthesis of hierarchically Co@C nanoarchitecture in heteroatom doped
723 porous carbons for oxidative degradation of emerging contaminants. *App. Catal. B:*
724 *Environ.* **2018**, *225*, 76-83.
- 725 28. Tian, X.; Gao, P.; Nie, Y.; Yang, C.; Zhou, Z.; Li, Y.; Wang, Y. A novel singlet oxygen
726 involved peroxymonosulfate activation mechanism for degradation of ofloxacin and
727 phenol in water. *Chem. Comm.* **2017**, *53*, (49), 6589-6592.
- 728 29. Yang, Z.; Dai, D.; Yao, Y.; Chen, L.; Liu, Q.; Luo, L. Extremely enhanced generation
729 of reactive oxygen species for oxidation of pollutants from peroxymonosulfate induced
730 by a supported copper oxide catalyst. *Chem. Eng. J.* **2017**, *322*, 546-555.
- 731 30. Jiang, M.; Lu, J.; Ji, Y.; Kong, D. Bicarbonate-activated persulfate oxidation of
732 acetaminophen. *Water Res.* **2017**, *116*, 324-331.
- 733 31. Khan, A.; Wang, H.; Liu, Y.; Jawad A.; Ifthikhar, J.; Liao, Z.; Wang, T.; Chen, Z. Highly
734 efficient $\alpha\text{-Mn}_2\text{O}_3@ \alpha\text{-MnO}_2$ -500 nanocomposite for peroxymonosulfate activation:
735 comprehensive investigation of manganese oxides *J. Mater. Chem. A*, **2018**, *6*, 1590–1600.
- 736 32. Yu, L.; Zhang, G.; Liu, C.; Lan, H.; Liu, H.; Qu, J. Interface stabilization of
737 undercoordinated iron centers on manganese oxides for nature-inspired peroxide
738 activation. *ACS Catal.* **2018**, *8* (2), 1090-1096.

- 739 33. Peng, W.; Liu, J.; Li, C.; Zong, F.; Xu, W.; Zhang, X.; Fang, Z.; A multipath
740 peroxymonosulfate activation process over supported by magnetic CuO-Fe₃O₄
741 nanoparticles for efficient degradation of 4-chlorophenol. *Korean J. Chem. Eng.* **2018**,
742 *35*, 1662–1672.
- 743 34. Saputra, E.; Muhammad, S.; Sun, H.; Ang, H. M.; Tadé, M. O.; Wang, S., Different
744 crystallographic one-dimensional MnO₂ nanomaterials and their superior performance
745 in catalytic phenol degradation. *Environ. Sci. Technol.* **2013**, *47*, (11), 5882-5887.
- 746 35. Brame, J.; Long, M.; Li, Q.; Alvarez, P. Trading oxidation power for efficiency:
747 differential inhibition of photo-generated hydroxyl radicals versus singlet oxygen.
748 *Water Res.* **2014**, *60*, 259–266.
- 749 36. Zhang, T.; Chen, W.; Ma, J.; Qiang, Z. Minimizing bromate formation with cerium
750 dioxide during ozonation of bromide-containing water. *Water Res.* **2008**, *42*, (14),
751 3651-3658.
- 752 37. Liang, C.; Huang, C. F.; Mohanty, N.; Kurakalva, R. M. A rapid spectrophotometric
753 determination of persulfate anion in ISCO. *Chemosphere* **2008**, *73* (9), 1540-1543.
- 754 38. Yuan, Z.; Lina W.; Junhua W.; Shuixin X.; Ping C.; Zhaoyin H.; Xiaoming Z.
755 Hydrogenolysis of glycerol over homogenously dispersed copper on solid base
756 catalysts. *App. Catal. B: Environ.* **2011**, *101*, 3, 431-440.
- 757 39. Van Der Grift, C. J. G.; Wielers, A. F. H.; Jogh, B. P. J.; Van Beunum, J.; De Boer, M.;
758 Versluijs-Helder, M.; Geus, J. W. Effect of the reduction treatment on the structure and
759 reactivity of silica-supported copper particles. *J. Catal.* **1991**, *131* (1), 178-189.
- 760 40. Zabilskiy, M.; Djinović, P.; Erjavec, B.; Dražić, G.; Pintar, A. Small CuO clusters on
761 CeO₂ nanospheres as active species for catalytic N₂O decomposition. *App. Catal. B:*
762 *Environ.* **2015**, *163*, 113-12.

- 763 41. Zhao, S.; Li, K.; Jiang, S.; Li, J. Pd–Co based spinel oxides derived from pd
764 nanoparticles immobilized on layered double hydroxides for toluene combustion. *App.*
765 *Catal. B: Environ.* **2016**, *181*, 236-248.
- 766 42. Deng, Y.; Handoko, A. D.; Du, Y.; Xi, S.; Yeo, B. S. In situ Raman spectroscopy of
767 copper and copper oxide surfaces during electrochemical oxygen evolution reaction:
768 identification of Cu^{III} oxides as catalytically active species. *ACS Catal.* **2016**, *6*, (4),
769 2473-2481.
- 770 43. Yun, E.T.; Lee, J. H.; Kim, J.; Park, H.D.; Lee, J. Identifying the nonradical mechanism
771 in the peroxymonosulfate activation process: singlet oxygenation versus mediated
772 electron transfer. *Environ. Sci. Technol.* **2018**, *52*, (12), 7032-7042.
- 773 44. Lee, H.; Kim, H. i.; Weon, S.; Choi, W.; Hwang, Y. S.; Seo, J.; Lee, C.; Kim, J. H.
774 Activation of persulfates by graphitized nanodiamonds for removal of organic
775 compounds. *Environ. Sci. Technol.* **2016**, *50*, (18), 10134-10142.
- 776 45. Duan, X.; Ao, Z.; Zhou, L.; Sun, H.; Wang, G.; Wang, S. Occurrence of radical and
777 nonradical pathways from carbocatalysts for aqueous and nonaqueous catalytic
778 oxidation. *App. Catal. B: Environ.* **2016**, *188*, 98-105.
- 779 46. Li, C.; Huang, Y.; Dong, X.; Sun, Z.; Duan, X.; Ren, B.; Zheng, S.; Dionysiou, D. D.,
780 Highly efficient activation of peroxymonosulfate by natural negatively-charged
781 kaolinite with abundant hydroxyl groups for the degradation of atrazine. *App. Catal.*
782 *B: Environ.* **2019**, *247*, 10-23.
- 783 47. Zhu, Z.S.; Yu, X.J.; Qu, J.; Jing, Y.Q.; Abdelkrim, Y.; Yu, Z.Z., Preforming abundant
784 surface cobalt hydroxyl groups on low crystalline flowerlike Co₃(Si₂O₅)₂(OH)₂ for
785 enhancing catalytic degradation performances with a critical nonradical reaction. *App.*
786 *Catal. B: Environ.* **2020**, *261*, 118238.

- 787 48. Guan, Y.H.; Ma, J.; Ren, Y.M.; Liu, Y.L.; Xiao, J.Y.; Lin, L.Q.; Zhang, C., Efficient
788 degradation of atrazine by magnetic porous copper ferrite catalyzed
789 peroxymonosulfate oxidation via the formation of hydroxyl and sulfate radicals.
790 *Water Res.* **2013**, *47*, (14), 5431-5438.
- 791 49. Ren, Y.; Lin, L.; Ma, J.; Yang, J.; Feng, J.; Fan, Z., Sulfate radicals induced from
792 peroxymonosulfate by magnetic ferrosipinel MFe_2O_4 (M=Co, Cu, Mn, and Zn) as
793 heterogeneous catalysts in the water. *App. Catal. B: Environ.* **2015**, *165*, 572-578.
- 794 50. Knözinger, E.; Jacob, K.H.; Singh, S.; Hofmann, P., Hydroxyl groups as IR active
795 surface probes on MgO crystallites. *Surf. Sci.* **1993**, *290*, (3), 388-402.
- 796 51. Del Arco, M.; Martin, C.; Martin, I.; Rives, V.; Trujillano, R., A FTIR spectroscopic
797 study of surface acidity and basicity of mixed Mg, Al-oxides obtained by thermal
798 decomposition of hydrotalcite. *Spectrochimica Acta Part A.* **1993**, *49*, (11), 1575-
799 1582.
- 800 52. Zhang, W.; Tay, H. L.; Lim, S. S.; Wang, Y.; Zhong, Z.; Xu, R., Supported cobalt
801 oxide on MgO: highly efficient catalysts for degradation of organic dyes in dilute
802 solutions. *App. Catal. B: Environ.* **2010**, *95*, (1), 93-99.
- 803 53. Xu, Y.; Ai, J.; Zhang, H., The mechanism of degradation of bisphenol A using the
804 magnetically separable $CuFe_2O_4$ /peroxymonosulfate heterogeneous oxidation process.
805 *J. Hazard. Mater.* **2016**, *309*, 87-96.
- 806 54. Lee, J.; Hong, S.; Mackeyev, Y.; Lee, C.; Chung, E.; Wilson, L. J.; Kim, J. H.; Alvarez,
807 P. J. Photosensitized oxidation of emerging organic pollutants by tetrakis C60
808 aminofullerene-derivatized silica under visible light irradiation. *Environ. Sci. Technol.*
809 **2011**, *45*, 10598–10604.

- 810 55. Duan, X.; Su, C.; Miao, J.; Zhong, Y.; Shao, Z.; Wang, S.; Sun, H. Insights into
811 perovskite-catalyzed peroxymonosulfate activation: Maneuverable cobalt sites for
812 promoted evolution of sulfate radicals. *App. Catal. B: Environ.* **2018**, *220*, 626-634.
- 813 56. Chai, X. S.; Hou, Q. X.; Luo, Q.; Zhu, J. Y. Rapid determination of hydrogen peroxide
814 in the wood pulp bleaching streams by a dual-wavelength spectroscopic method. *Anal.*
815 *Chim. Acta* **2004**, *507* (2), 281-284.
- 816 57. Zabilskiy, M.; Djinović, P.; Tchernychova, E.; Tkachenko, O. P.; Kustov, L. M.; Pintar,
817 A. Nanoshaped CuO/CeO₂ materials: effect of the exposed ceria surfaces on catalytic
818 activity in N₂O decomposition reaction. *ACS Catal.* **2015**, *5*, (9), 5357-5365.
- 819 58. Wang, L.; Sun, Y. G.; Hu, L. L.; Piao, J. Y.; Guo, J.; Manthiram, A.; Ma, J.; Cao, A.
820 M. Copper-substituted Na_{0.67}Ni_{0.3-x}Cu_xMn_{0.7}O₂ cathode materials for sodium-ion
821 batteries with suppressed P₂-O₂ phase transition. *J. Mater. Chem. A* **2017**, *5*, (18),
822 8752-8761.
- 823 59. Lindsey, M. E.; Tarr, M. A. Inhibition of hydroxyl radical reaction with aromatics by
824 dissolved natural organic matter. *Environ. Sci. Technol.* **2000**, *34* (3), 444-449.
- 825 60. Wang, L.; Jiang, J.; Pang, S. Y.; Zhou, Y.; Li, J.; Sun, S.; Gao, Y.; Jiang, C. Oxidation
826 of bisphenol A by nonradical activation of peroxymonosulfate in the presence of
827 amorphous manganese dioxide. *Chem. Eng. J.* **2018**, *352*, 1004-1013.
- 828 61. Tratnyek, P. G.; Hoigne, J. Oxidation of substituted phenols in the environment: a
829 QSAR analysis of rate constants for reaction with singlet oxygen. *Environ. Sci. Technol.*
830 **1991**, *25*, (9), 1596-1604.
- 831 62. Guan, C.; Jiang, J.; Pang, S.; Luo, C.; Ma, J.; Zhou, Y.; Yang, Y. Oxidation kinetics of
832 bromophenols by nonradical activation of peroxydisulfate in the presence of carbon
833 nanotube and formation of brominated polymeric products. *Environ. Sci. Technol.*
834 **2017**, *51*, (18), 10718-10728.

- 835 63. Tekle-Röttering, A.; von Sonntag, C.; Reisz, E.; Eyser, C. v.; Lutze, H. V.; Türk, J.;
836 Naumov, S.; Schmidt, W.; Schmidt, T. C. Ozonation of anilines: Kinetics,
837 stoichiometry, product identification and elucidation of pathways. *Water Res.* **2016**, *98*,
838 147-159.
- 839 64. Sun, S.; Liu, Y.; Ma, J.; Pang, S.; Huang, Z.; Gu, J.; Gao, Y.; Xue, M.; Yuan, Y.; Jiang,
840 J. Transformation of substituted anilines by ferrate(VI): Kinetics, pathways, and effect
841 of dissolved organic matter. *Chem. Eng. J.* **2018**, *332*, 245-252.

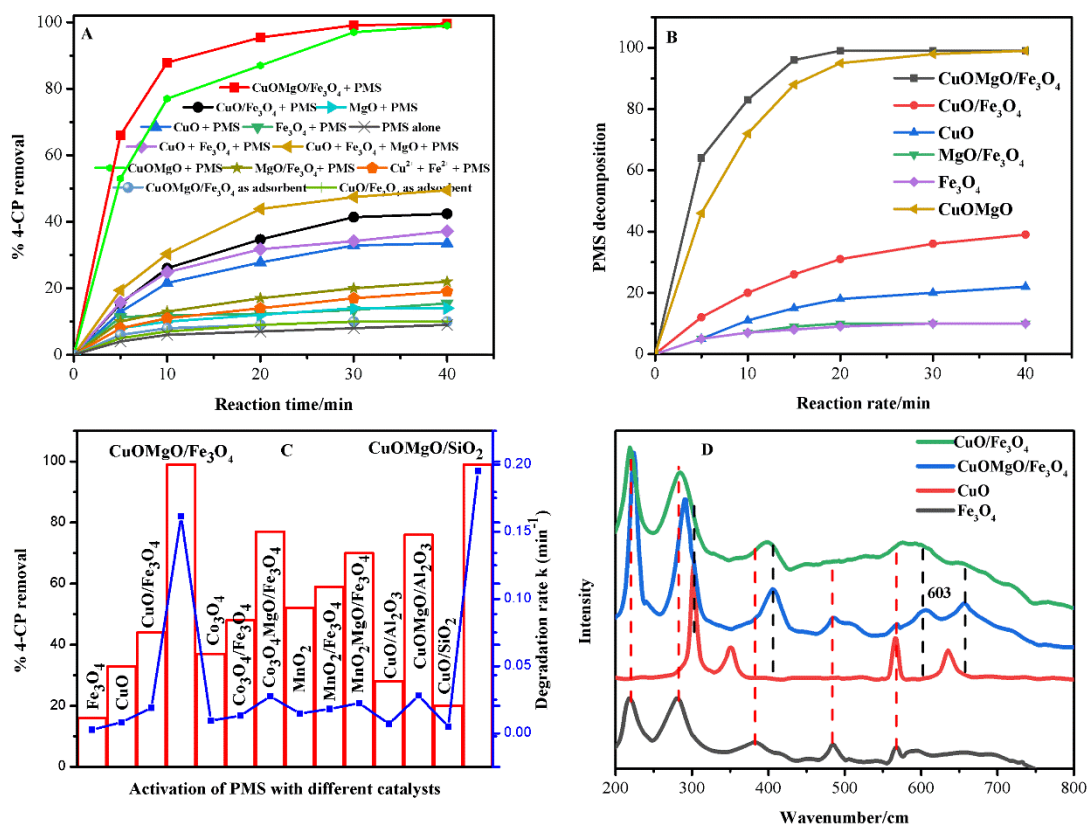
842

843

844

845

846

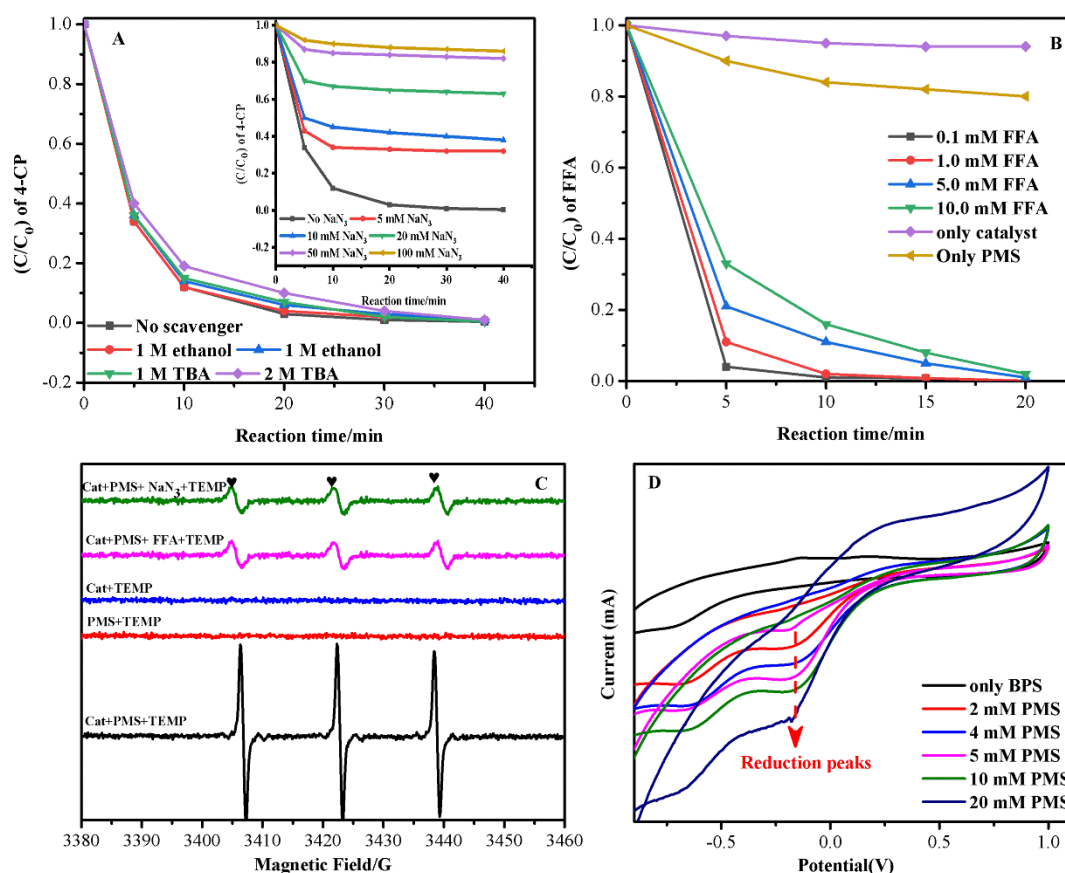


847

848 **Figure 1** (A-C) role of MgO to improve the catalytic activity and PMS utilization efficiency
 849 of different metals oxides (D) Raman spectra showing the abundant lattice defects and
 850 prominent peak of Cu³⁺ state in CuOMgO/Fe₃O₄ catalyst.

851 **Conditions:** 4-CP 40 ppm, PMS 2 mM, catalyst 0.2g/L, reaction temperature 30 °C and
 852 reaction time 40 min.

853



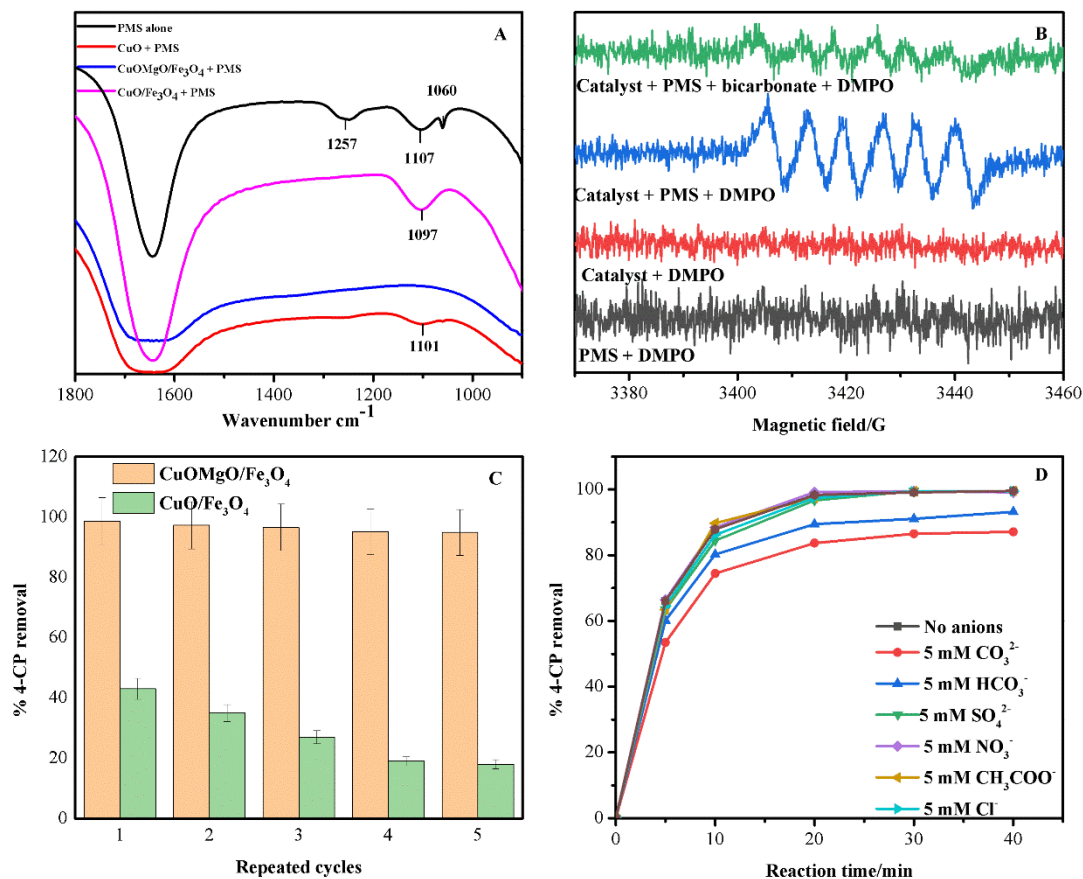
854

855 **Figure 2** (A) Influences of ethanol and TBA on the activity of CuOMgO/Fe₃O₄, (inset showing
 856 the influence of NaN_3 on the activity of CuOMgO/Fe₃O₄ (B) degradation of FFA as $^1\text{O}_2$ -
 857 indicator (C) generation of $^1\text{O}_2$ with TEMP (D) CV plots showing the increase in the reduction
 858 peak of CuOMgO/Fe₃O₄+PMS system with increasing PMS amount.

859 **Conditions:** 4-CP 40 ppm, PMS 2 mM, catalyst 0.2g/L, reaction temperature 30 °C and
 860 reaction time 40 min.

861

862



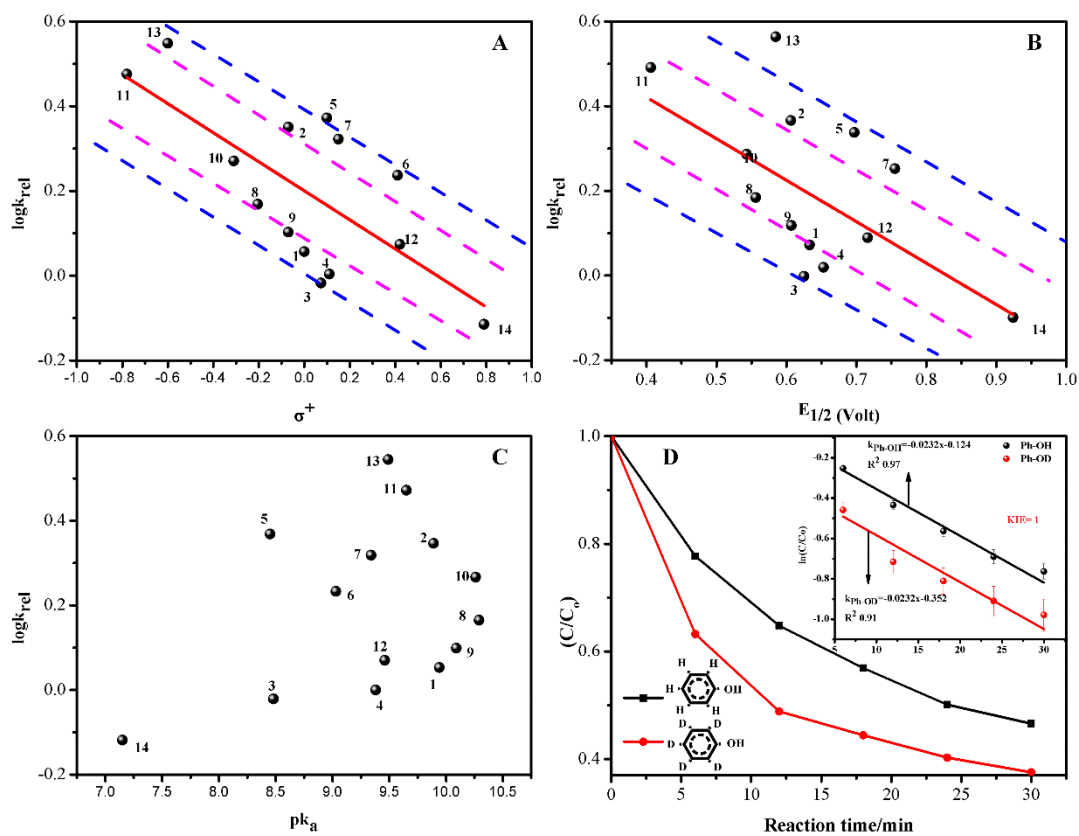
863

864 **Figure 3** (A) ATR-FTIR spectra of PMS after interacting CuOMgO/Fe₃O₄, CuO/Fe₃O₄ and865 CuO catalysts (B) generation of DMPO-O₂ adduct in ethanol, giving strong evidence for the866 presence of super oxides in CuOMgO/Fe₃O₄+PMS system (C) stability of CuOMgO/Fe₃O₄,867 CuO/Fe₃O₄ in the recycled experiments (D) influence of anions on the catalytic activity of868 CuOMgO/Fe₃O₄+PMS system.

869

870

871



872

873 **Figure 4** Quantitative structure-activity relationships of substituted phenols for (A) Hammett
 874 σ^+ constant, (B) half-wave potential ($E_{1/2}$) (C) pK_a and (D) Calculating KIE using
 875 CuOMgO/Fe₃O₄+PMS system.

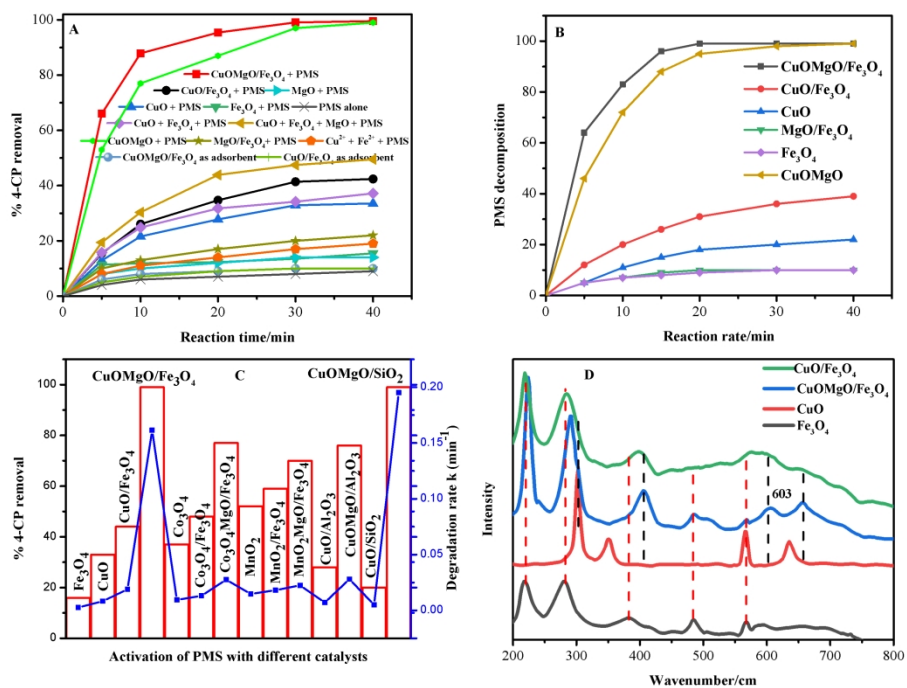


Fig.1 (A-C) role of MgO to improve the catalytic activity and PMS utilization efficiency of different metals oxides (D) Raman spectra showing the abundant lattice defects and prominent peak of Cu³⁺ state in CuOMgO/Fe₃O₄ catalyst. Conditions: 4-CP 40 ppm, PMS 2 mM, catalyst 0.2g/L, reaction temperature 30 oC and reaction time 40 min.

216x159mm (400 x 400 DPI)

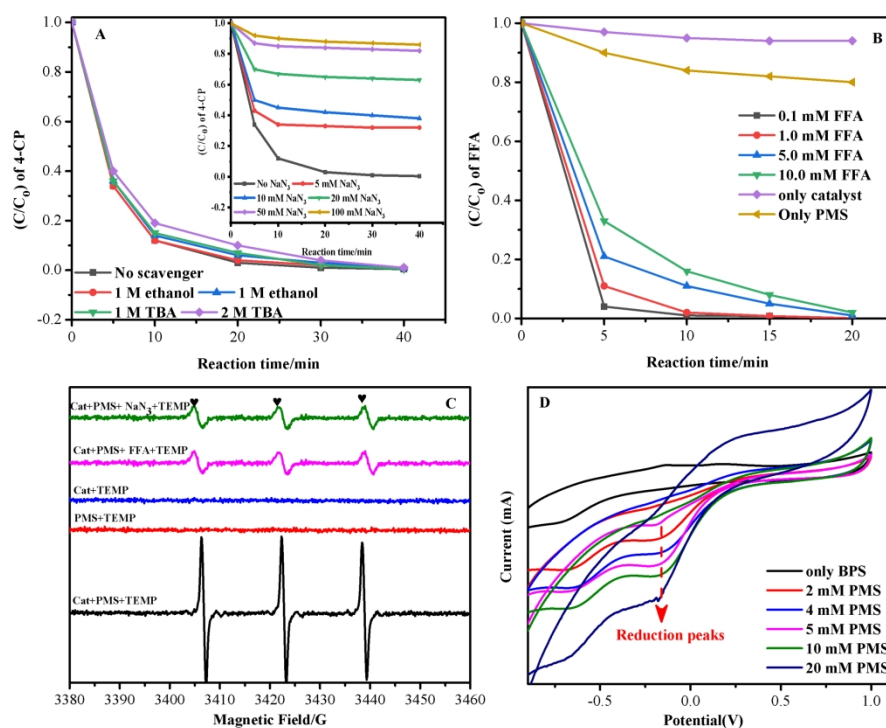


Fig. 2 (A) Influences of ethanol and TBA on the activity of CuOMgO/Fe₃O₄, (inset showing the influence of Na₂S₂O₃ on the activity of CuOMgO/Fe₃O₄) (B) degradation of FFA as $1O_2^-$ indicator (C) generation of $1O_2$ with TEMP (D) CV plots showing the increase in the reduction peak of CuOMgO/Fe₃O₄+PMS system with increasing PMS amount.

Conditions: 4-CP 40 ppm, PMS 2 mM, catalyst 0.2g/L, reaction temperature 30 °C and reaction time 40 min.

203x159mm (400 × 400 DPI)

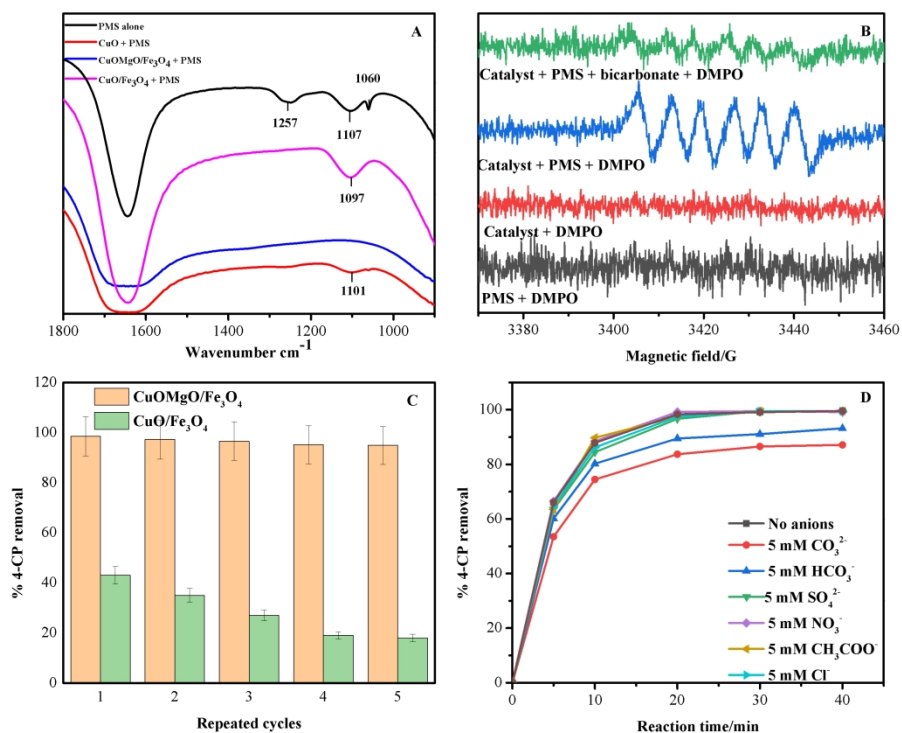


Fig. 3 (A) ATR-FTIR spectra of PMS after interacting CuOMgO/Fe₃O₄, CuO/Fe₃O₄ and CuO catalysts (B) generation of DMPO-O₂ adduct in ethanol, giving strong evidence for the presence of super oxides in CuOMgO/Fe₃O₄+PMS system (C) stability of CuOMgO/Fe₃O₄, CuO/Fe₃O₄ in the recycled experiments (D) influence of anions on the catalytic activity of CuOMgO/Fe₃O₄+PMS system.

204x160mm (400 x 400 DPI)

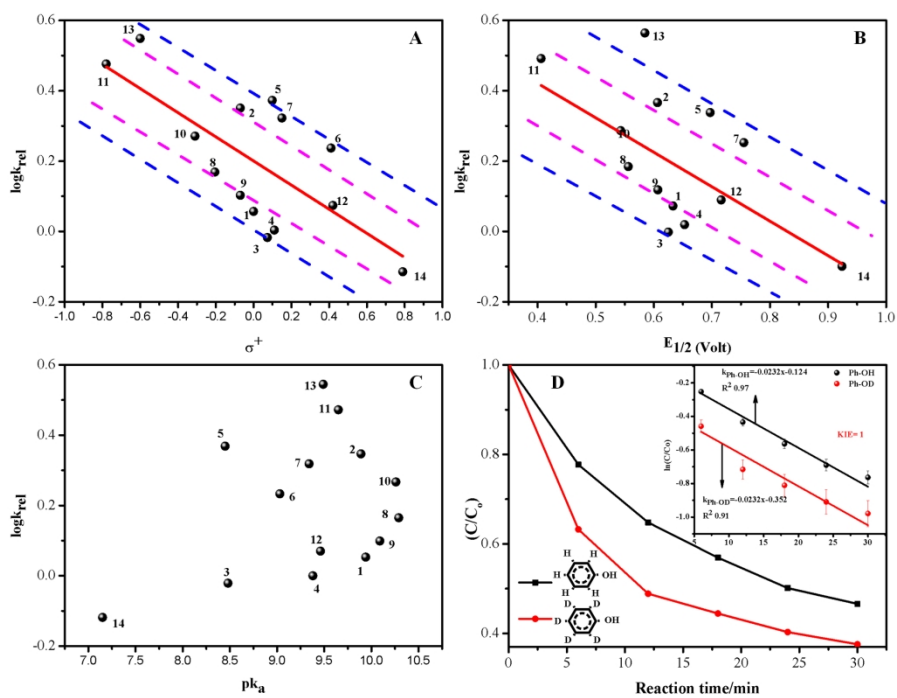


Figure 4 Quantitative structure-activity relationships of substituted phenols for (A) Hammett ρ^+ constant, (B) half-wave potential ($E_{1/2}$) (C) pKa and (D) Calculating KIE using CuOMgO/Fe₃O₄+PMS system.

221x163mm (300 x 300 DPI)